

AN ABSTRACT OF THE THESIS OF

Diana Delgado for the degree of Master of Science in Electrical and Computer Engineering presented on June 10, 2010.

Title: Iterative Reconstruction Methods of CT Images Using a Statistical Framework.

Abstract approved:

Raviv Raich

Medical imaging technologies play a vital role in early diagnosis of disease by providing internal images of the human body to medical professionals. Computed Tomography (CT) is currently the most commonly used medical imaging technology because it is easy to use, detectors and scanners are constantly improving, and more importantly, patients receive less radiation compared to other imaging technologies. This thesis focuses on improving CT reconstruction algorithms by incorporating prior knowledge of the tissues being scanned. A Gaussian Mixture Prior, and Gibbs sampling is introduced into the reconstruction framework and solved using Maximum-a-posterior (MAP). As a comparison, the images were also reconstructed using unregularized and regularized Maximum Likelihood (ML).

©Copyright by Diana Delgado
June 10, 2010
All Rights Reserved

Iterative Reconstruction Methods of CT Images Using a Statistical Framework

by
Diana Delgado

A THESIS

submitted to

Oregon State University

in partial fulfillment of
the requirements for the
degree of

Master of Science

Presented June 10, 2010
Commencement June 2011

Master of Science thesis of Diana Delgado presented on June 10, 2010

APPROVED:

Major Professor, representing Electrical and Computer Engineering

Director of the School of Electrical Engineering and Computer Science

Dean of the Graduate School

I understand that my thesis will become part of the permanent collection of Oregon State University libraries. My signature below authorizes release of my thesis to any reader upon request.

Diana Delgado, Author

ACKNOWLEDGEMENTS

I would like to thank my major Professor, Dr. Raich for all of his help throughout the research and writing process of this thesis. Thank you to the professors that served on my defense committee: Dr. Annette von Jouanne, Dr. Huaping Liu and Dr. Karen Shell, your comments and suggestions were very helpful. I would also like to give a special thanks to my parents, Fidel and Carmen Delgado, without their constant support, and motivation none of this would be possible. My parents have always encouraged me to follow my dreams, to constantly keep my mind active by learning something new every day, and to be a kind, honest, sincere individual. They have been such wonderful role models and mentors in my life; I strive to be like them each day. I would also like to thank my boyfriend, John Yen who has always been a constant source of encouragement; he always knows how to make me smile. Thank you to my sisters, Karen and Carmen for always believing in me and looking out for me. Also, a very special thank you to my nephews and niece: Richie, Max and Veronica, who with their unconditional love, giggles and smiles bring so much joy into my life. I am so blessed to have such an amazing family. Finally thank you to the rest of my family and of course, my closest friends for always being there for me.

TABLE OF CONTENTS

	<u>Page</u>
1	Introduction 1
1.1	Computed Tomography..... 1
1.2	Thesis Outline..... 3
2	Fundamentals of Computed Tomography..... 4
2.1	X-ray Generation and Detection..... 4
2.2	Simple Reconstruction Methods for CT..... 5
2.2.1	Radon Transform and Fourier Slice Theorem..... 5
2.2.2	Filtered Parallel Beam Backprojection..... 8
3	The Inverse Problem 10
3.1	Inverse Problem..... 10
3.2	System Operators..... 11
3.2.1	Forward Operator 11
3.2.2	Adjoint Operator..... 13
3.3	Image Noise..... 14
3.3.1	Noise Models..... 14
3.3.2	Image Artifacts 15
3.3.2.1	Beam Hardening..... 15
3.3.2.2	Partial Volume Effects 16
3.3.2.3	Photon Starvation 16
3.3.2.4	Undersampling 16
3.3.2.5	Patient Artifacts..... 16

TABLE OF CONTENTS (Continued)

	<u>Page</u>
3.4 Classical Solutions.....	17
3.4.1 Unregularized Maximum Likelihood	17
3.4.2 Regularized Maximum Likelihood.....	18
4 Incorporating a Gaussian Mixture Prior	21
4.1 MAP with Gaussian Mixture Prior	21
4.1.1 The Prior	21
4.1.2 The Likelihood	24
4.2 Gibbs Sampling	27
5 Simulations.....	32
5.1 Image Reconstruction Framework.....	32
5.1.1 Shepp Logan Phantom.....	32
5.1.2 Real CT Image.....	34
5.2 Unregularized Maximum Likelihood	35
5.3 Regularized Maximum Likelihood.....	35
5.4 MAP with Gaussian Mixture Prior	36
5.5 Gibbs Sampling Prior	39
6 Results	41
6.1 Shepp Logan Phantom.....	41
6.2 Real CT Image.....	49
7 Conclusions	55

TABLE OF CONTENTS (Continued)

	<u>Page</u>
7.1 Future Work.....	55
Bibliography	57
Appendix A – Maximum Likelihood.....	61
A.1 Unregularized Maximum Likelihood.....	61
A.2 Regularized Maximum Likelihood	63
Appendix B - MAP-GMP	64

LIST OF FIGURES

<u>Figure</u>	<u>Page</u>
Figure 2.1: Radon Transform of a circle for $\theta = 0^\circ$	6
Figure 2.2: Graphical Representation of the Fourier Slice Theorem, which relates the FT of a projection to the FT of the object along a radial line [7].	7
Figure 3.1: Block Diagram of the Forward Operator, H . Takes as input an image $f(x, y)$ and outputs a sinogram $P(\theta, t)$	12
Figure 3.2: Block Diagram of the Adjoint Operator, H^T . Takes as input a sinogram $P(\theta, t)$ and outputs a reconstructed image $f(x, y)$	13
Figure 3.3: Sinogram (Projection Data).....	14
Figure 4.1: Example of a simple Gaussian Prior for 2 tissues, bone and muscle and air. 23	23
Figure 5.1: 128x128 Shepp Logan Phantom.....	32
Figure 5.2: 512x512 CT Scan of the human heart (From [4]).	34
Figure 5.3: 128x128 portion of the human heart. A vertebrae and part of the aorta can be seen in the image.....	34
Figure 5.4: Histogram of the CT Heart Image with Gaussian Distributions	38
Figure 6.2: Gibbs Sampling Reconstruction, 10 iterations	43
Figure 6.3: Gibbs Sampling Reconstruction, 1000 iterations	43
Figure 6.4: Gibbs Sampling, optimal σ_s . $\text{SNR}_{\text{ORIGINAL}} = 46.6 \text{ dB}$, $\text{SNR}_{\text{RECONSTRUCTED}} = 35.3069 \text{ dB}$	46
Figure 6.5: MAP Reconstruction, optimal σ_s . $\text{SNR}_{\text{ORIGINAL}} = 46.6 \text{ dB}$, $\text{SNR}_{\text{RECONSTRUCTED}} = 18.3595 \text{ dB}$	46
Figure 6.6: Regularized ML, $\lambda \rightarrow 0$, $\text{SNR}_{\text{ORIGINAL}} = 46.6 \text{ dB}$, $\text{SNR}_{\text{RECONSTRUCTED}} = 12.8479 \text{ dB}$	46
Figure 6.7: Regularized ML, λ_{opt} , $\text{SNR}_{\text{ORIGINAL}} = 46.6 \text{ dB}$, $\text{SNR}_{\text{RECONSTRUCTED}} = 13.0463$	46
Figure 6.8: Unregularized ML, $\text{SNR}_{\text{ORIGINAL}} = 46.6 \text{ dB}$, $\text{SNR}_{\text{RECONSTRUCTED}} = 12.6784 \text{ dB}$	46

LIST OF FIGURES (Continued)

<u>Figure</u>	<u>Page</u>
Figure 6.9: Gibbs Sampling, optimal σ_s . $\text{SNR}_{\text{ORIGINAL}}=26.6$ dB, $\text{SNR}_{\text{RECONSTRUCTED}} = 13.2021$ dB.....	47
Figure 6.10: MAP Reconstruction, optimal σ_s . $\text{SNR}_{\text{ORIGINAL}}= 26.6$ dB, $\text{SNR}_{\text{RECONSTRUCTED}} = 13.225$ dB	47
Figure 6.11: Regularized ML, $\lambda \rightarrow 0$, $\text{SNR}_{\text{ORIGINAL}}= 26.6$ dB, $\text{SNR}_{\text{RECONSTRUCTED}} = 10.401$ dB.....	47
Figure 6.12: Regularized ML, λ_{opt} , $\text{SNR}_{\text{ORIGINAL}}= 26.6$ dB, $\text{SNR}_{\text{RECONSTRUCTED}} = 11.3646$ dB.....	47
Figure 6.13: Unregularized ML, $\text{SNR}_{\text{ORIGINAL}}= 26.6$ dB, $\text{SNR}_{\text{RECONSTRUCTED}} = -4.1653$ dB.....	47
Figure 6.14: Gibbs Sampling, optimal σ_s . $\text{SNR}_{\text{ORIGINAL}} = 7.5$ dB, $\text{SNR}_{\text{RECONSTRUCTED}} = 2.4363$ dB.....	48
Figure 6.15: MAP Reconstruction, optimal σ_s . $\text{SNR}_{\text{ORIGINAL}} = 7.5$ dB, $\text{SNR}_{\text{RECONSTRUCTED}} = 2.8989$ dB.....	48
Figure 6.16: Regularized ML, $\lambda \rightarrow 0$, $\text{SNR}_{\text{ORIGINAL}} = 7.5$ dB, $\text{SNR}_{\text{RECONSTRUCTED}} = 0.86642$ dB.....	48
Figure 6.17: Regularized ML, λ_{opt} , $\text{SNR}_{\text{ORIGINAL}} = 7.5$ dB, $\text{SNR}_{\text{RECONSTRUCTED}} = 2.9225$ dB.....	48
Figure 6.18: Unregularized ML, $\text{SNR}_{\text{ORIGINAL}} = 7.5$ dB, $\text{SNR}_{\text{RECONSTRUCTED}} = -24.2185$ dB.....	48
Figure 6.19: $\text{SNR}_{\text{RECONSTRUCTED}}$ vs. $\text{SNR}_{\text{ORIGINAL}}$ for the CT Image of the human heart, using 5 different methods.....	51
Figure 6.20: Gibbs Sampling, optimal σ_s . $\text{SNR}_{\text{ORIGINAL}} = 54.8$ dB, $\text{SNR}_{\text{RECONSTRUCTED}} = 22.3419$ dB.....	52
Figure 6.21: MAP Reconstruction, optimal σ_s . $\text{SNR}_{\text{ORIGINAL}} = 54.8$ dB, $\text{SNR}_{\text{RECONSTRUCTED}} = 25.9815$ dB.....	52
Figure 6.22: Regularized ML, $\lambda \rightarrow 0$, $\text{SNR}_{\text{ORIGINAL}} = 54.8$ dB, $\text{SNR}_{\text{RECONSTRUCTED}} = 32.323$ dB.....	52

LIST OF FIGURES (Continued)

<u>Figure</u>	<u>Page</u>
Figure 6.23: Regularized ML, λ_{opt} , $SNR_{ORIGINAL} = 54.8$ dB, $SNR_{RECONSTRUCTED} = 32.2658$ dB.....	52
Figure 6.24: Unregularized ML, $SNR_{ORIGINAL} = 54.8$ dB, $SNR_{RECONSTRUCTED} = 6.4731$ dB.....	52
Figure 6.25: Gibbs Sampling, optimal σ_s . $SNR_{ORIGINAL} = 34.8$ dB, $SNR_{RECONSTRUCTED} = 17.2853$ dB.....	53
Figure 6.26: MAP Reconstruction, optimal σ_s . $SNR_{ORIGINAL} = 34.8$ dB, $SNR_{RECONSTRUCTED} = 19.7247$ dB.....	53
Figure 6.27: Regularized ML, $\lambda \rightarrow 0$, $SNR_{ORIGINAL} = 34.8$ dB, $SNR_{RECONSTRUCTED} = 20.94$ dB.....	53
Figure 6.28: Regularized ML, λ_{opt} , $SNR_{ORIGINAL} = 34.8$ dB, $SNR_{RECONSTRUCTED} = 22.2201$ dB.....	53
Figure 6.29: Unregularized ML, $SNR_{ORIGINAL} = 34.8$ dB, $SNR_{RECONSTRUCTED} = -13.5526$ dB.....	53
Figure 6.30: Gibbs Sampling, optimal σ_s . $SNR_{ORIGINAL} = 14.9$ dB, $SNR_{RECONSTRUCTED} = 9.5479$ dB.....	54
Figure 6.31: MAP Reconstruction, optimal σ_s . $SNR_{ORIGINAL} = 14.9$ dB, $SNR_{RECONSTRUCTED} = 3.2036$ dB.....	54
Figure 6.32: Regularized ML, $\lambda \rightarrow 0$, $SNR_{ORIGINAL} = 14.9$ dB, $SNR_{RECONSTRUCTED} = -1.7491$ dB.....	54
Figure 6.33: Regularized ML, λ_{opt} , $SNR_{ORIGINAL} = 14.9$ dB, $SNR_{RECONSTRUCTED} = 11.9609$ db.....	54
Figure 6.34: Unregularized ML, $SNR_{ORIGINAL} = 14.9$ dB, $SNR_{RECONSTRUCTED} = -33.4604$ dB.....	54

LIST OF TABLES

<u>Table</u>	<u>Page</u>
Table 4.1: Attenuation Values for Main Human Tissues (From [1])	22
Table 5.1: Variance of the noise added to the sinograms in the simulations.....	33
Table 5.2: Optimal Values for σ_x for the R-ML for both the Shepp Logan and CT Heart Image.....	36
Table 5.3: Optimal μ_s and σ_s values for the Shepp Logan Phantom using MAP-GMP Reconstruction	37
Table 5.4: Optimal μ_s and σ_s values for the Heart CT Image using MAP-GMP Reconstruction	38
Table 5.5: Optimal σ_s values for the Gibbs Reconstruction for the Shepp Logan Phantom.	39
Table 5.6: Optimal σ_s values for the Gibbs Reconstruction for the Heart CT Image	40

1 Introduction

1.1 Computed Tomography

Computed Tomography (CT) is a method of producing a 2-D or 3-D image of the internal structures of a solid object, such as the human body. These images are produced by recording how waves or particles change as they pass through the object. All CT methods analyze a series of cross-sectional scans made along a single axis of the object and then a 2-D/3-D image of the structure is constructed. Several computer imaging methods exist today such as Magnetic Resonance Imaging (MRI), Positron Emission Tomography (PET), and CT. Unlike CT, MRI uses a strong magnetic field, radio frequency pulses and a computer to produce a detailed image of the inside of the body. PET differs from CT and MRI since it is a nuclear imaging technology which uses a camera and a tracer (radioactive material) to look at the internal structures of the body. CT is currently the most widely used imaging method because they are easy to use, detector technologies and algorithms are continuously improving, and objects are exposed to less radiation than MRI or PET.

In CT, different types of algorithms are used to recover the cross sectional image of an object from its projection data. The absorption of x-rays by the different internal structures of the object being illuminated results in an image of the inside of the object. The projection data is the information derived from the energies that are transmitted through the object at different angles relative to the position of the object. At each angle, the object is illuminated by an energy source, such as x-rays. The energy propagates through the object and is collected by a series of detectors, as shown in Figure 1.1; this makes up one projection. The process is repeated until a series of projections at different angles are collected. A projection at a certain angle is the integral of the image at that particular angle. Depending on the configuration or set-up of the source and detectors, the projection data can be found in many different ways, hence there are many reconstruction frameworks. The most common reconstruction frameworks include: parallel-beam, fan-beam, and cone-beam

projections. Parallel beam projections is the simplest of the three to understand and implement, this is the set-up assumed in this thesis. In fan-beam and cone-beam projections the geometry of the set-up changes relative to the parallel beam projections; however, the fundamental theorems for reconstruction remain the same.

Research on reconstruction algorithms is ongoing, currently some of the popular topics for image reconstruction algorithms include: the incorporation/use of sparsity through total variation, spatial correlation among pixels (incorporating the idea of neighborhoods), and multi-resolution reconstruction algorithms [1][2][3]. Sparsity takes into account where the gradient of the image is zero; from this assumption fewer projections and a higher quality image can be reconstructed. Multiresolution reconstruction methods aim to decrease the reconstruction time by reconstructing images of a lower resolution. Research is also being done on the denoising problem, which reduces noise from the reconstructed image through filtering techniques or histogram equalization [4].

This thesis primarily deals with iterative reconstruction methods of CT images using a statistical framework. The motivation behind this thesis is the medical application of CT tomography. CT is used in clinical diagnosis to detect abnormalities such as cancer, tumors, or organ deficiencies. One main concern with CT in medicine is the radiation dosage the patient receives during a scan versus the accuracy of the reconstructed image. A low radiation generally produces a lower quality image than when higher amounts of radiation are used, hence the need for improved reconstruction techniques. With better reconstruction methods, random noise that occur during the acquisition process are reduced, and higher quality images are produced. This allows for good tissue identification (for medical diagnosis), and patients are exposed to less radiation.

1.2 Thesis Outline

In section 2, a brief discussion on the fundamentals of computed tomography is presented. The section gives an overview of the physics, more specifically generation and detection techniques. In addition, fundamental theorems and a basic reconstruction method are presented; all of which are necessary to understanding the reconstruction process.

Next, the framework of the inverse problem is presented in the context of image reconstruction along with two of the dominant noise models, Gaussian and Poisson. The two noise models are used to describe the noise present in the data obtained from a CT scanner. The model and benefits of each are discussed along with why a Gaussian model was chosen in the reconstruction algorithms used throughout this thesis. The inverse problem requires the use of a forward and inverse operator; these were implemented in MATLAB and detailed further in Section 3. A classical solution to the inverse problem is Maximum Likelihood; both the Unregularized Maximum Likelihood (U-ML) and Regularized Maximum Likelihood (R-ML) are presented.

In Section 4, the use of a prior which is consistent with tissue density distributions found in medical literature is proposed and used in the reconstruction process. The prior uses the prior knowledge of CT attenuation values for tissues of the human body. Each tissue attenuation value is represented as a Gaussian function and a Maximum-a-posteriori (MAP) approach is used to solve for the reconstructed image. Gibbs Sampling is also incorporated into the MAP reconstruction to improve the quality of the reconstructed image.

All of these CT methods were implemented in MATLAB and tested using a standard Shepp Logan Phantom and a dicom CT image with noise added to the sinogram of each image. The results are presented and discussed in Section 6. Finally, future methods to improve the algorithms presented in this thesis are proposed in Section 7.

2 Fundamentals of Computed Tomography

2.1 X-ray Generation and Detection

X-ray tomography consists of emitting x-rays at an object from multiple orientations (angles) relative to the object and measuring the decrease in x-ray intensity along a series of linear paths. X-rays are generated with an x-ray tube. An x-ray tube consists of three parts, an anode, a vacuum, and a cathode. The cathode emits electrons into the vacuum, creating a current. Next, high voltage (~30-150kV) is applied to the anode and cathode which accelerates the electrons, causing them to collide with the anode material (usually made from tungsten or molybdenum) [5]. These collisions result in the release/emittance of energy in the form of an EM wave (~10-0.01 nanometers) [5].

X-rays are detected by a series of radiation detectors (sensors) that measure x-ray intensity attenuation. These detectors can be configured in a wide variety of ways in order to create optimal CT-scanners configurations, such as parallel-beam, fan-beam, and cone-beam.

The Lambert-Beer Law gives the equation for a monochromatic x-ray beam through a homogenous material:

$$I = I_0 e^{-\mu x}, \quad (1.1)$$

where, I_0 is the input intensity of an x-ray, I , is the output intensity of an x-ray, μ is the materials linear attenuation coefficient (measured in cm^{-1}) and x is the distance traveled by the ray [6]. Equation 1.1 assumes μ is constant over the interval x , but in the real world this is not the case. Typically, the object doing the attenuation is composed of different materials, such as in the human body. In the human body, different tissue types, such as muscle, and fat have different attenuation coefficients. If an object consists of multiple materials, μ can be considered as being a function of

the coordinates x and y , therefore denoting it as $\mu(x, y)$, hence the relationship between I and I_0 becomes the following:

$$I = I_0 \exp\left(-\int_{ray} \mu(x, y) ds\right), \quad (1.2)$$

or, equivalently:

$$P(\theta, t) = \int_{ray} \mu(x, y) ds = \ln\left(\frac{I}{I_0}\right), \quad (1.3)$$

where ds , is an element of length along a the radiations path and t is the normal representation of a line perpendicular to the line of the radiations path [6]. The left hand side is a ray integral for a projection $P(\theta, t)$. In CT, $P(\theta, t)$, is the projection measurement/data and the log of the input x-ray intensity over the output x-ray intensity represents the line integral of the attenuation coefficients along the x-ray path.

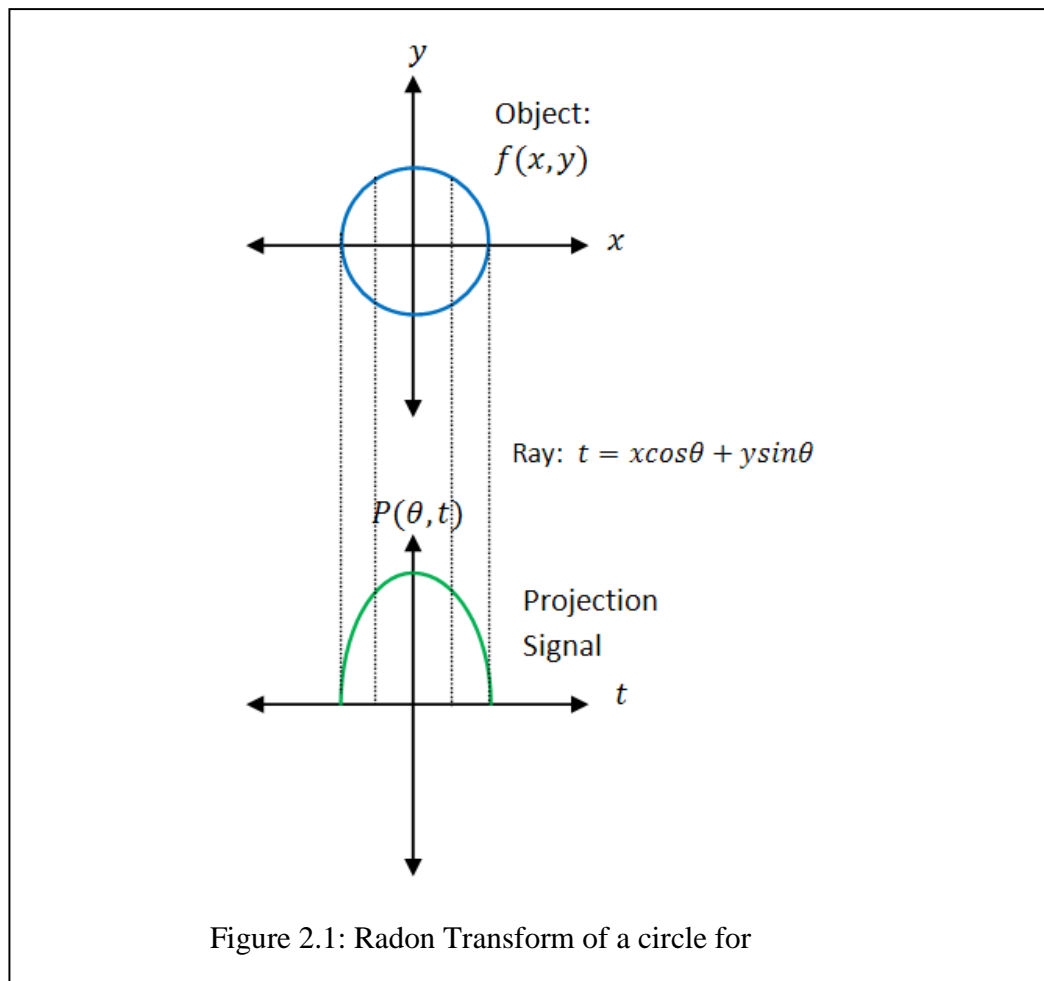
2.2 Simple Reconstruction Methods for CT

2.2.1 Radon Transform and Fourier Slice Theorem

Parallel projections can be represented mathematically by the following equation:

$$P(\theta, t) = \int_{-\infty}^{\infty} \int_{-\infty}^{\infty} f(x, y) \delta(x \cos \theta + y \sin \theta - t) dx dy, \quad (2.1)$$

where, $f(x, y)$ represents the attenuation of x-rays at location (x, y) , θ is a given projection angle, t is the detector location and δ is the delta function [7]. The function $P(\theta, t)$ is the projection of $f(x, y)$ at angle θ , which is the integral of $f(x, y)$ along a line $t = x \cos \theta + y \sin \theta$ and is called the Radon Transform of $f(x, y)$. This is depicted at $\theta = 0^\circ$ in Figure 2.1.



The Fourier transform (FT) of the object is defined as:

(2.2)

and the FT of the projection is the following:

(2.3)

then by the Fourier Slice Theorem, the FT of a projection is related to the FT of the object along radial lines:

(2.4)

By taking the projections and FT of the object function $f(x, y)$ at different angles of θ , the values of $F(u, v)$ along radial lines, such as line BB, can be determined as depicted in Figure 2.2.

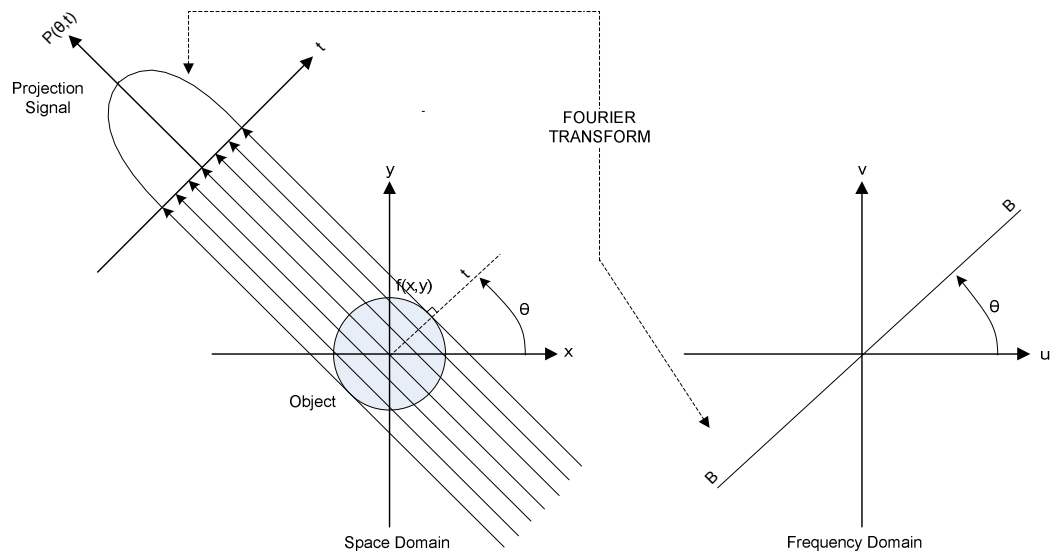


Figure 2.2: Graphical Representation of the Fourier Slice Theorem, which relates the FT of a projection to the FT of the object along a radial line [7].

If an infinite number of projections are taken, then $F(u, v)$ would be known at all points in the $u - v$ plane, hence the object $f(x, y)$ can be recovered by using the inverse FT:

$$f(x, y) = \int_{-\infty}^{\infty} \int_{-\infty}^{\infty} F(u, v) e^{j2\pi(ux+vy)} du dv. \quad (2.5)$$

This would be the simplest reconstruction method where all of the reconstructions from each angle are summed to recover the final image of the object. The main issue that results in reconstructing $f(x, y)$ in this manner is that there is only partial information about its FT, having a limited number of lines going through the origin (spectral lines) and not the entire 2D frequency domain.

2.2.2 Filtered Parallel Beam Backprojection

Each projection is a nearly independent measurement of the object. The filtered backprojection (FBP) algorithm involves two steps: the filtering step which involves the weighting of each projection in the frequency domain and the backprojection step that involves the elemental reconstruction corresponding to each filtered projection.

Recalling the formula for the inverse FT Equation 2.5, and converting to polar coordinates (ω, θ) by making the following substitutions:

$$u = \omega \cos \theta, \quad (2.6)$$

$$v = \omega \sin \theta, \quad (2.7)$$

and changing the differentials by:

$$dudv = \omega d\omega d\theta, \quad (2.8)$$

Equation 2.5, becomes:

$$\begin{aligned} f(x, y) &= \int_0^{2\pi} \int_{-\infty}^{\infty} F(\omega \cos \theta, \omega \sin \theta) e^{j2\pi\omega(x \cos \theta + y \sin \theta)} \omega d\omega d\theta \end{aligned} \quad (2.9)$$

By splitting this into two integrals, one for θ ranging from $0^\circ - 180^\circ$ and the other $180^\circ - 360^\circ$ and using the property $F(\omega, \theta + 180^\circ) = F(-\omega, \theta)$ the expression can be written as:

$$f(x, y) = \int_0^\pi \left[\int_{-\infty}^{\infty} F(\omega \cos \theta, \omega \sin \theta) |\omega| e^{j2\pi\omega t} d\omega \right] d\theta, \quad (2.10)$$

where, as before $t = x \cos \theta + y \sin \theta$ [6][7].

The inner expression is the inverse 1-D FT of the projection data with the added term $|\omega|$ which is a 1-D filter function. This filter function is a ramp filter and is usually band-limited when using this approach to solve for $f(x, y)$.

For parallel-beam back projections, multiple projections at different angles are needed to obtain a high quality reconstructed image exposing the patient to potentially

a harmful dose of radiation. For this reason, fan-beam or cone-beam geometry is used to obtain the projections. The principle of the FBP algorithm remains the same, only the geometry changes. Fewer projections are needed to reconstruct the image using these two methods.

Like the simple reconstruction in Equation 2.5, the quality of the filtered backprojection depends on how many projections you have of the image; the more projections the better the quality of the reconstructions. It also does not take into account physical noise from the CT scanner that affects the measured attenuation values, hence resulting in a noisy image.

3 The Inverse Problem

Before discussing the inverse problem, solutions and algorithms throughout this thesis the notation used from here on will first be explained. The unavailable image (or reconstructed image) that is being solved for, $f(x, y)$ is now represented as x :

$$x = \text{vec}(\mathbf{F}), \quad \mathbf{F} = f(x, y) = \begin{pmatrix} f(x_1, y_1) & \cdots & f(x_N, y_1) \\ \vdots & \ddots & \vdots \\ f(x_1, y_N) & \cdots & f(x_N, y_N) \end{pmatrix}. \quad (3.1)$$

In this case, $f(x, y)$ is an $N \times N$ image that can be represented as an $N^2 \times 1$ vector, x , where each element in the vector represents one pixel. The $\text{vec}(\mathbf{F})$ is a column by column concatenation of \mathbf{F} . The value associated with that pixel is the CT attenuation value for the particular tissue the pixel represents. The total number of pixels in the image will be represented as n , where $n = N \times N$.

The sinogram data, $P(\theta, t)$ is now represented as, y and like x can be represented as a matrix.

$$y = \text{vec}(\mathbf{P}), \quad \mathbf{P} = P(\theta, t) = \begin{pmatrix} P(\theta_1, t_1) & \cdots & P(\theta_1, t_L) \\ \vdots & \ddots & \vdots \\ P(\theta_M, t_1) & \cdots & P(\theta_M, t_L) \end{pmatrix}. \quad (3.2)$$

The sinogram data results in a $M \times L$ image, which can be represented as a vector, \mathbf{P} , where each element in the vector represents one pixel and the value associated with that pixel is the log ratio of the relation shown in Equation 1.3, hence the sum of $f(x, y)$ along the line $t = x \cos \theta + y \sin \theta$. From this point on x and y will no longer be referred to as coordinates; x will be the reconstructed image that is being solved for and y the sinogram data that is used to solve for x . The total number of pixels in the sinogram will be represented as m , where $m = M \times L$.

3.1 Inverse Problem

Without accounting for noise, the reconstruction problem involves solving the following inverse problem:

$$y = Hx. \quad (3.3)$$

This problem can be solved by inverting the transformation, H , to obtain the estimate, \hat{x} , of the original distribution x :

$$\hat{x} = H^{-1}y. \quad (3.4)$$

The problem with this solution is that the forward transformation, H , is often singular or nearly singular, hence, for a given set of projection data there may be many or no solutions, thus, x , and the inverse of H may not exist. Also in the cases where H^{-1} exists, the matrix is too large to compute and if the projection data has noise then it becomes an ill-posed problem.

In the case of image reconstruction, H , the forward operator maps the image space to the projection space; it essentially performs the radon transform. Since we cannot apply the inverse to find the image, we apply the adjoint operator, H^T , to the projection data:

$$\hat{x} = H^T y. \quad (3.5)$$

note that $H^{-1} \neq H^T$, and H^T , the adjoint operator is analogous to applying the backprojection to y (the projection data) to obtain an estimate of x (the image) [8]. The forward and adjoint operator are used extensively throughout this thesis to develop more optimal algorithms. The reconstruction algorithms developed use statistical methods, since they succeed even in situations where projections are missing, inconsistent, or a large amount of noise is present. The forward and adjoint operators and the noise found in images are described in more details in the sections that follow.

3.2 System Operators

3.2.1 Forward Operator

The forward operator H , was developed in order to simulate the function of a CT Scanner. The raw data of a CT scanner from the x-ray detectors, sinogram is the projection data in radon space. Since we do not have raw data from a CT scanner, we

simulate it by developing the forward operator, H . The operator takes in an $N \times N$ image and returns the sinogram of the image. The block diagram in Figure 3.1 describes the step by step process of the forward operator:

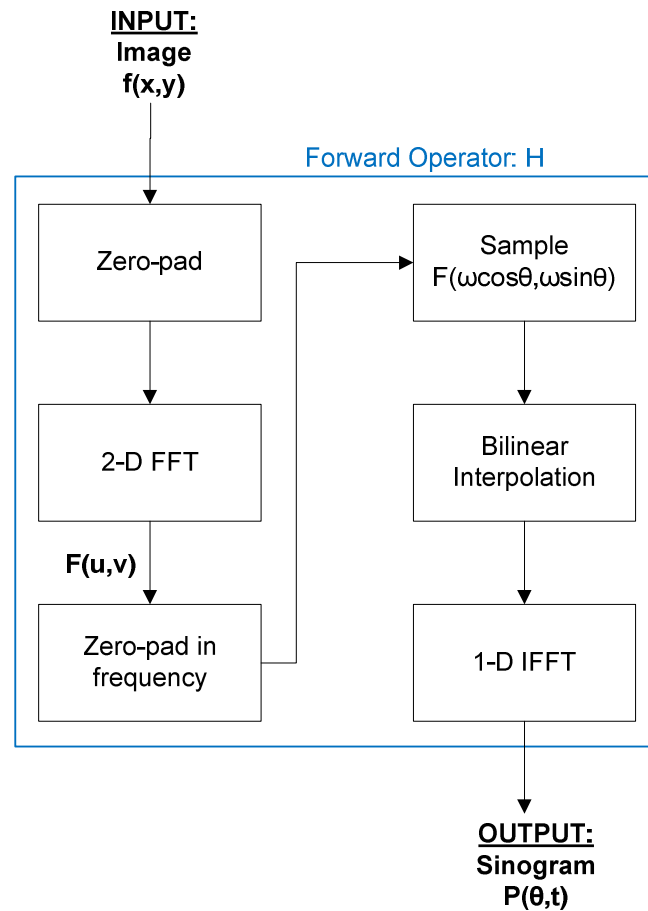


Figure 3.1: Block Diagram of the Forward Operator, H . Takes as input an image $f(x,y)$ and outputs a sinogram $P(\theta,t)$.

The image is first zero-padded to the next power of 2, in order to not lose any information when converting it to the frequency domain. Next the 2D Fourier Transform of the zero-padded image is taken, this essentially sums the pixels at a given angle and results in radial lines in the frequency domain at that particular angle. The FT of the image is then zero-padded to $\sqrt{2}N$ which is the diagonal length of the image, so no points along the radial lines are lost. The FT of the image is then sampled

at $(\omega \cos \theta, \omega \sin \theta)$, resulting in $F(\omega \cos \theta, \omega \sin \theta)$. Since everything was implemented with vectors and matrices when sampling at $(\omega \cos \theta, \omega \sin \theta)$ indefinite points could not be indexed, hence bilinear interpolation was performed on the indexed values. Finally the 1-D inverse (fast) Fourier transform (IFFT) of the interpolated $F(\omega \cos \theta, \omega \sin \theta)$ is taken resulting in the projection of $f(x, y)$, $P(\theta, t)$.

3.2.2 Adjoint Operator

The adjoint operator, H^T , essentially performs the opposite of the forward operator. H^T was implemented and the block diagram of the adjoint is shown in Figure 3.2.

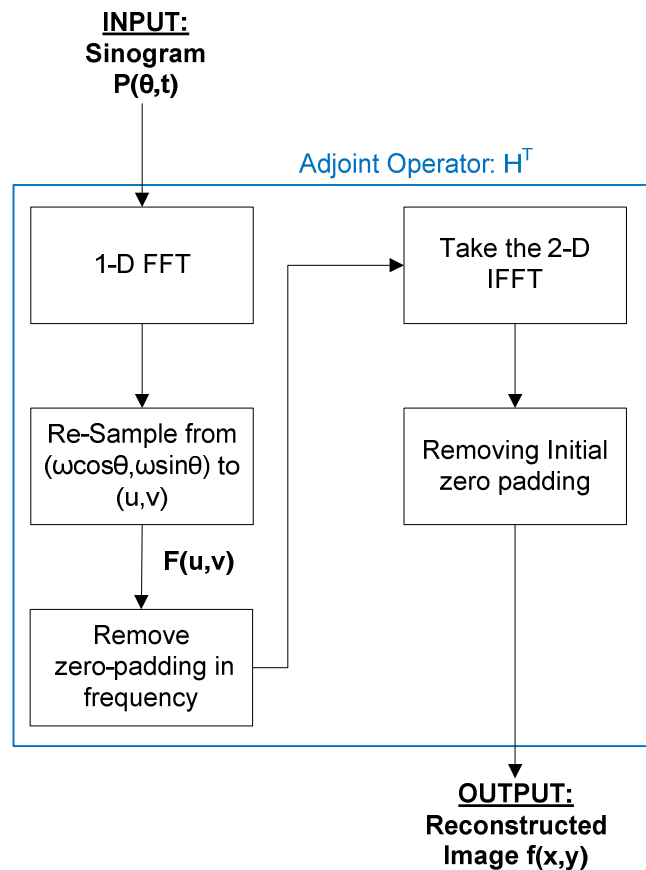


Figure 3.2: Block Diagram of the Adjoint Operator, H^T . Takes as input a sinogram $P(\theta, t)$ and outputs a reconstructed image $f(x, y)$.

As seen in the block diagram above, first the 1-D (fast) Fourier Transform (FFT) is taken of the projection data (sinogram), next it is mapped back to the (u,v) space. A typical sinogram is shown in Figure 3.3.

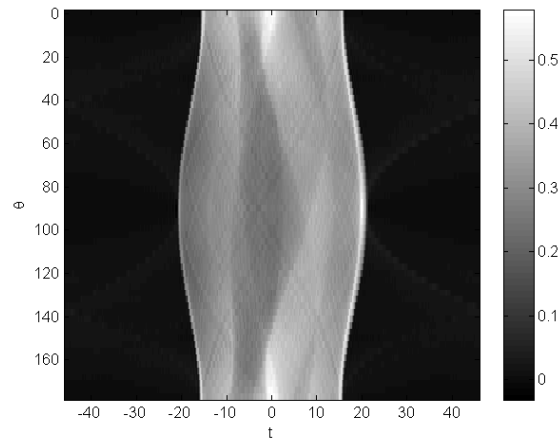


Figure 3.3: Sinogram (Projection Data)

The zero padding in the frequency domain is removed and the 2-D IFFT is taken of . Finally the zero padding in the space is removed, which results in a reconstructed image of .

3.3 Image Noise

X-ray CT images suffer from different kinds of noise and image artifacts. The most significant source of noise for these images occurs in the detection process: how photon detections are modeled. Artifacts can occur from the physics of the system such as beam-hardening, partial volume effects, photon starvation, undersampling, or from patient artifacts. This section discusses image noise and briefly describes image artifacts.

3.3.1 Noise Models

Image noise occurs with the statistical fluctuation of photon detection. This noise can be modeled in two different ways, as Gaussian noise or Poisson noise.

The general form of a Poisson distribution can be written as:

$$P(Y = y) = \frac{\lambda^y e^{-\lambda}}{y!}, \quad y \geq 0, \quad (3.6)$$

where, $P(Y = y)$ is the probability of a random variable Y , of value y and having a mean of λ . The variance of the distribution is proportional to the average number of photons since photons are not emitted or detected uniformly. The mean and variance of a Poisson distribution are identical, hence the signal to noise ratio is proportional to the square root of the detector measurement counts. Using this noise model is very attractive for this reason; it produces a much better signal-to-noise ratio (SNR) since it models the measurement more precisely.

The form of the Gaussian distribution is as follows:

$$P(Y = y) = \frac{1}{(\sqrt{2\pi\sigma^2})^m} e^{-\frac{\|y-Hx\|^2}{2\sigma^2}}, \quad (3.7)$$

where, μ is the mean of the distribution and σ^2 is the variance. In this case the noise and variance are different and y , the number of photon counts, is not proportional to the variance; hence the distribution is impartial to high or low intensities.

Although the Poisson Noise model provides a better model for the noise in CT reconstruction it is very difficult to work with. Gaussian models are more commonly used since they are much more tractable; they are easier to solve and control.

3.3.2 Image Artifacts

Several different types of image artifacts occur in image reconstruction, some of the main artifacts are discussed in the following sections.

3.3.2.1 Beam Hardening

As an x-ray passes through an object, the lower energy photons are absorbed much quicker than the higher energy photons, the beam is said to become “harder”. This physical phenomenon of the CT system causes two types of artifacts, cupping artifacts and dark bands or streaks. As the beam becomes harder the rate at which it attenuates

decreases so when it reaches the detector the intensities are much higher than expected [5][6].

3.3.2.2 Partial Volume Effects

Partial volume effects occur when a dense tissue/object is lying off center to the width of the beam. This causes the beam to diverge resulting in shading artifacts in the reconstructed image. These artifacts can be avoided by changing the width of the beam [5][6].

3.3.2.3 Photon Starvation

Photon starvation occurs with objects that are very dense (highly attenuate), such as bone. When the x-ray is travelling through this dense object, most of the photons are absorbed and very little reach the detectors. This results in very noisy projections that produce horizontal streaks in the image. A very quick solution to this problem is to increase the power of the x-ray beam; however, this not very favorable for the patient since they will be subjected to intense radiation [5][6].

3.3.2.4 Undersampling

If too few projections are taken then there is not enough information to reconstruct a good quality image; recall that the more projections, the better the image quality. If too few projections are taken then aliasing occurs and fine stripes appear in the reconstructed image, which can be problematic in some diagnostic situations where fine details are needed [5][6].

3.3.2.5 Patient Artifacts

There are two types of patient artifacts that occur, artifacts caused by metallic objects or by patient motion. Metallic objects such as dental fillings and prosthetic devices are extremely dense and have high attenuation values. Therefore, very little EM waves pass through to the detectors causing extreme streaking in the image and loss of information since the projection is no longer complete. Patient motion can

cause misregistration of attenuation values; these artifacts can occur as shading or slight streaking in the entire image [5][6].

3.4 Classical Solutions

3.4.1 Unregularized Maximum Likelihood

In Maximum Likelihood (ML) we minimize the following objective function:

$$\min_x p(y|x), \quad (3.8)$$

where y is modeled as being a Gaussian distribution with a mean of Hx , and standard deviation of σ_n^2 , $y \sim N(Hx, \sigma_n^2 I)$, hence the cost function can be defined as:

$$p(y|x) = \frac{1}{(\sqrt{2\pi\sigma_n^2})^m} e^{-\frac{\|y-Hx\|^2}{2\sigma_n^2}}, \quad (3.9)$$

where, y is the projection data (sinogram), H is the forward operator (radon transform of x), and σ_n the standard deviation of the noise on y . The negative log likelihood function of the above equation simplifies to:

$$L(x) = -\log(p(y|x)) = \frac{\|y - Hx\|^2}{2\sigma_n^2} + \frac{m}{2} \log(2\pi\sigma_n^2). \quad (3.10)$$

The classical least squares solution to 3.10 results in the following:

$$x = (H^T H)^{-1} H^T y. \quad (3.11)$$

This solution is not an optimal solution and is also computationally expensive; hence we use an optimization transfer approach to solve for 3.10. With optimization transfer we transfer minimization from the log likelihood $L(x)$ to a surrogate function $G(x, x^k)$, this transfer is successful since the following conditions hold [9]:

$$\begin{aligned} 1) \quad & L(x) \leq G(x, x^k) \quad \forall x, x^k, \\ 2) \quad & L(x^k) = G(x^k, x^k). \end{aligned} \quad (3.12)$$

Through optimization transfer we replace equation 3.8 with the following [9]:

$$x^{k+1} = \min_x G(x, x^k). \quad (3.13)$$

This is done by replacing x in 3.9 with $x^k - x^{k+1} + x^{k+1}$ and solving 3.8, this results in the following iterative solution (see appendix A .1 for a more detailed solution):

$$x^{k+1} = x^k - \frac{1}{\alpha} (H^T (y - Hx^k)), \quad (3.14)$$

where α is a convergence term and by Jensen's inequality we restrict α to be ,

$$\alpha = \frac{\|H(y - Hx^k)\|^2}{\|(x^{k+1} - x^k)\|^2}. \quad (3.15)$$

In order to speed up the convergence process a two-step ML was used:

$$x^{k+1} = x^k + c_1 \left(\frac{x^k + x^{k+1}}{\|H(x^{k+1} - x^k)\|} \right) + c_2 \left(\frac{H^T (y - Hx^k)}{\|H(H^T (y - Hx^k))\|} \right), \quad (3.16)$$

where c_1 and c_2 can found by solving the following equation:

$$\begin{bmatrix} c_1 \\ c_2 \end{bmatrix} = \begin{bmatrix} 1 & (Hv_1)^T (Hv_2) \\ v_1(H^T(y - Hx^k)) & 1 \end{bmatrix}^{-1} \times \begin{bmatrix} v_1(H^T(y - Hx^k)) & v_2(H^T(y - Hx^k)) \end{bmatrix}. \quad (3.17)$$

These resulting values for c_1 and c_2 , are then substituted into 3.10 to solve for the reconstructed image, x .

As can be seen by Equation 3.14, the unregularized ML minimizes the error term $(y - Hx)$ so it does not take into account what range of values the pixels in the image should be in; hence when there is noise in the sinogram, the reconstructed image deteriorates as the iterations are increased. For this reason, ML needs to be regularized.

3.4.2 Regularized Maximum Likelihood

With image reconstruction there are more parameters than there are equations, hence when unregularized ML is used we do not give preference to any solution, by

regularizing it we give preference to the low energy equations. This restricts the values of the reconstructed image, thus allowing it not to deteriorate as the iterations are increased. In the regularized ML case we use a maximum a posteriori (MAP) reconstruction with an added l_2 regularization to solve for the reconstructed image, x . With MAP we try to minimize the following function:

$$\min_x p(y|x)p(x), \quad (3.18)$$

where,

$$p(y|x) = \frac{1}{(\sqrt{2\pi\sigma_n^2})^m} e^{-\frac{\|y-Hx\|^2}{2\sigma_n^2}}. \quad (3.19)$$

and

$$p(x) = \frac{1}{(\sqrt{2\pi\sigma_x^2})^n} e^{-\frac{\|x\|^2}{2\sigma_x^2}}. \quad (3.20)$$

where, σ_x^2 is the variance of the reconstructed image, x . Ignoring the terms that do not depend on x , up to a constant, the negative log-likelihood of the above equation simplifies to [8]:

$$-\log(p(y|x)p(x)) = \frac{1}{2\sigma_n^2} (\|y - Hx\|^2 + \lambda\|x\|^2), \quad (3.21)$$

where the regularization term, λ , equals the following:

$$\lambda = \frac{\sigma_n^2}{\sigma_x^2}. \quad (3.22)$$

Now minimize Equation 3.19 to solve for x :

$$\min_x \|y - Hx\|^2 + \lambda\|x\|^2. \quad (3.23)$$

The classical least squares solution to this equations results in the following:

$$x = (H^T H + \lambda I)^{-1} H^T y. \quad (3.24)$$

We cannot use this solution since we do not know the inverse of the term $(H^T H + \lambda I)$, this quantity would be impossible to compute computationally and the inverse of this

quantity may not exist [8]. Solving this through optimization transfer results in the following solution for x :

$$x^{k+1} = \frac{c}{c + \lambda} \left(x^k + \frac{1}{c} H^T (y - Hx^k) \right), \quad (3.25)$$

where, c , the convergence constant is restricted to be the following:

$$c^{k+1} = \frac{\|H(H^T(y - Hx^k) - \lambda x^k)\|^2}{\|(H^T(y - Hx^k) - \lambda x^k)\|^2}. \quad (3.26)$$

By the addition of the regularization constant, λ , we take this term to be very close to zero, $\lambda \rightarrow 0$. Even with the smallest addition of λ , the eigenvalues of Equation 3.22 are prevented from going to infinite, thus regularizing the ML reconstruction. For a more complete solution see Appendix A.2.

Regularized Maximum Likelihood constrains the tissue values to be within a defined range. It prevents an over or underestimate of values; it also continues to minimize the error as in the unregularized case. Some of the problems that arise with a regularized ML are that it is very general, it does not differentiate between the different tissues, and negative tissue values can be obtained.

4 Incorporating a Gaussian Mixture Prior

In the case of tomography, there is prior knowledge of what to expect with each CT slice of the human body. Although the size of each person varies, the internal structures remain the same, we know the tissues, tissue attenuation values and percentage of different tissues that should appear in each segment of the human body. This information can be found from medical tables. This prior information of tissue values is incorporated into a Gaussian mixture prior and by using maximum-a-posteriori (MAP) to solve, a more accurate image is reconstructed.

4.1 MAP with Gaussian Mixture Prior

4.1.1 The Prior

A Gaussian Mixture Prior (GMP) was introduced in order to improve the reconstruction of the image. Each tissue in the human body has a range at which it attenuates, the attenuation values in Hounsfield units and in cm^{-1} are shown for some of the main tissues in the human body in Table 4.1.

Table 4.1: Attenuation Values for Main Human Tissues (From [1])

Tissue	Attenuation Values			
	Min (HU)	Max (HU)	Min (1/cm)	Max (1/cm)
Soft Tissue	-120	220	0.016192	0.022448
Water	-5	10	0.018308	0.018584
Transudate	16	24	0.0186944	0.0188416
Intestine	5	35	0.018492	0.019044
Adrenal Gland	10	25	0.018584	0.01886
Kidney	20	40	0.018768	0.019136
Exudate	20	30	0.018768	0.018952
Heart	20	50	0.018768	0.01932
Tumor	21	51	0.0187864	0.0193384
Spleen, Muscle	40	50	0.019136	0.01932
Pancreas	30	50	0.018952	0.01932
Blood	50	60	0.01932	0.019504
Thyroid	60	80	0.019504	0.019872
Liver	60	70	0.019504	0.019688
Blood (Curdled)	70	90	0.019688	0.020056
Air	-1000		0	0.00184
Lung	-900	-500	0.00184	0.0092
Fat	-200	-60	0.01472	0.017296
Mamma	-100	-50	0.01656	0.01748
Parenchymatous Organs	10	90	0.018584	0.020056
Cancellous Bone	50	230	0.01932	0.022632
Bone	250	1000	0.023	0.0368
soft tissue	40	80	0.019136	0.019872
muscle	10	40	0.018584	0.019136

Typically the body parts being scanned by the CT scanner are known; hence, the tissue types that occur in those portions of the body are also known. Knowing the tissues types that are expected in each scan and the tissue attenuation ranges, a prior can be constructed with this information in order to solve for the reconstructed image using a MAP algorithm. These tissues can be represented as a series of Gaussian functions where the mean of each tissue occurs where the known attenuation values of those tissues lie, and the standard deviation of the Gaussian function can be based on

how much the attenuation value of the tissue varies from the mean chosen. All of these Gaussian functions together constitute the Gaussian Mixture Prior (GMP). Take for example a CT image containing only 2 tissues, bone, muscle, and air; the prior would then be chosen to be a set of three Gaussian functions. According to Table 4.1, the mean of air would be 0, bone would occur at 0.0368, and muscle at 0.021896. The standard deviation was chosen to be 0.006 for each of the Gaussian functions, this value allowed the functions to be wide enough to encompass a large range of tissue values. Figure 4.1, shows a graph of these Gaussian functions.

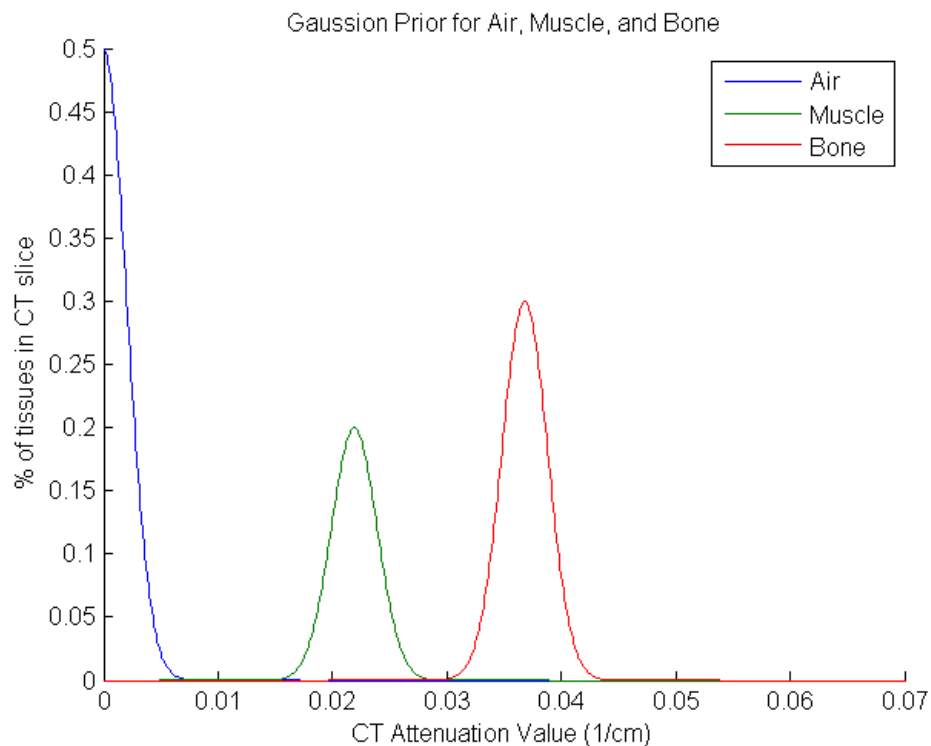


Figure 4.1: Example of a simple Gaussian Prior for 2 tissues, bone and muscle and air.

The standard deviation of these Gaussian functions can vary in order to obtain more optimal results. The wider the Gaussians the more tissue values the prior allows, the narrower the Gaussians the more selective the prior becomes, allowing less and less tissue values to be permitted in the reconstructed image.

Having a prior made up of more than one Gaussian function causes the prior to be non-convex; meaning there can be more than one optimal solution to the problem. The prior may also allow the solution to be trapped in a local minima instead of converging to the global minima. For example, a tissue value may be estimated as being tissue type A even though it is tissue type B and it may take several thousand iterations until it switches from type A to type B.

4.1.2 The Likelihood

Using Bayes' theorem we can incorporate this prior information in the estimation process of the reconstructed image. One possible estimate for the reconstructed image x and the estimation of s , is the maximum a posteriori (MAP) estimate [10]:

$$\operatorname{argmin}_{(x,s)} P(x, y, s|a),$$

$$\operatorname{argmin}_{(x,s)} p(y|x)p(x|s)p(s|a), \quad (4.1)$$

$$\operatorname{argmin}_{(x,s)} \log p(y|x) + \log p(x|s) + \log p(s|a), \quad (4.2)$$

where, the joint probability of (X,Y) can be written as:

$$p(y|x) = \prod_{i=1}^N \frac{1}{\sqrt{2\pi\sigma_x^2}} e^{-\frac{(y_i-(Hx)_i)^2}{2\sigma_x^2}}. \quad (4.3)$$

where, σ_x is the standard deviation of the image x . The prior can be incorporated as the following joint probability distribution of x and s , dependent on the model parameters s :

$$p(x|s) = \prod_{i=1}^N \prod_{s=1}^S p(x_i|s_i = s)^{I(s_i=s)}, \quad (4.4)$$

where $I(s)$, is an indicator function that maps each pixel to a certain tissue, s , where $s = \{1, 2, \dots, S\}$, and S is the total number of tissues that occur in the image that are to be represented in the GMP. Rewriting 4.4:

$$p(x|s) = \prod_{i=1}^N \prod_{s=1}^S \left(\frac{1}{\sqrt{2\pi\sigma_s^2}} e^{-\frac{(x_i-\mu_s)^2}{2\sigma_s^2}} \right)^{I(s_i=s)}, \quad (4.5)$$

where μ_s , is the mean of each tissue value, and σ_s is the standard deviation of each tissue value. In the prior what percentage of tissue occurs in the reconstructed image is taken into account, this is represented by the probability of x given a , where a is the percentage of occurrence of each tissue, and the equation is as follows:

$$p(\mathbf{s}|a) = \prod_{i=1}^N p(s_i|a) = \prod_{i=1}^N \prod_{s=1}^S a_s^{I(s_i=s)}, \quad (4.6)$$

hence,

$$\sum_{s=1}^S a_s = 1, \quad (4.7)$$

the percentage of occurrence of each tissue in the reconstructed image, sums to one.

Solving equation 4.2 with respect to x yields the following analytical solution:

$$x = 2 \left(\frac{H^T H}{\sigma_x^2} + D \right)^{-1} \left(\frac{H^T y}{\sigma_x^2} + D \mu_s \right), \quad (4.8)$$

where the matrix, μ_s , is a $N \times N$ images, each pixel of that image contains a value of μ to which that pixel is mapped to by the indicator function $I(s)$. For example if the indicator function determines pixel (1,1) of the reconstructed image to be of type tissue #2, $s = 2$, then the values assigned to that pixel would be μ_2 and σ_2 . The matrix D , is a diagonal matrix with σ_s along the diagonal. Although this is a solution for x we are unable to utilize it because the inverse of $\left(\frac{H^T H}{\sigma_x^2} + D \right)$ is unknown, since the matrix is too large or it does not exist. Hence, we use optimization transfer to solve 4.2, the iterative solution is as follows:

$$x^{k+1} = x^k + \frac{1}{c} \left(\left(\frac{H^T y}{\sigma_x^2} + D \mu_s \right) - \left(\frac{H^T H}{\sigma_x^2} + D \right) x^k \right). \quad (4.9)$$

By the Rayleigh Quotient c is defined as:

$$c = \frac{(x^{k+1} - x^k)^T \left(\frac{H^T H}{\sigma_x^2} + D \right) (x^{k+1} - x^k)}{\|x^{k+1} - x^k\|^2}. \quad (4.10)$$

Now that we have a solution for x , we must solve for the selection matrix S of the indicator function I , minimizing 4.2 with respect to s_i :

$$\begin{aligned} \min_{s_i} \sum_{s=1}^S \sum_{i=1}^N \frac{(x_i - \mu_s)^2}{2\sigma_s^2} I(s_i = s) \\ + \sum_{s=1}^S \left(\sum_{N=1}^N I(s_i = s) \right) \log \left(\frac{1}{as} \right) + \sum_{s=1}^S \frac{n_2}{2} \log \sigma_s^2. \end{aligned} \quad (4.11)$$

This results in a discrete equation that simplifies to the following solution of s_i for all $i = \{1, 2, \dots, S\}$:

$$s_i = \arg \min_{s=1,2,\dots,S} \frac{\log(\sigma_s^2)}{2} + \frac{(x_i - \mu_s)^2}{2\sigma_s^2} - \log a_s \quad (4.12)$$

once all of the S possible solutions for s_i are found, the minimum value of s_i is taken for each individual pixel. The resulting selection matrix, s_i , is then used to find μ_s and σ_s , two matrices containing the corresponding mean and standard deviation for each pixel of the image. For a more complete solution see Appendix B.

In order for the algorithm to converge more quickly a two-step MAP was found:

$$\begin{aligned} x^{k+1} = x^k + z_1 \frac{(b - Ax^k)}{\sqrt{(b - Ax^k)^T A (b - Ax^k)}} \\ + z_2 \frac{(x^{k-1} - x^k)}{\sqrt{(x^{k-1} - x^k)^T A (x^{k-1} - x^k)}}, \end{aligned} \quad (4.13)$$

where,

$$A = \left(\frac{H^T H}{\sigma_x^2} + D \right), \quad (4.14)$$

$$b = \left(\frac{H^T y}{\sigma_x^2} + D\mu_s \right), \quad (4.15)$$

and z_1 and z_2 are solved for by the following matrix equation:

$$\begin{bmatrix} z_1 \\ z_2 \end{bmatrix} = [V^T A V]^{-1} \begin{bmatrix} v_1 \\ v_2 \end{bmatrix} (b - Ax^k). \quad (4.16)$$

These resulting values for z_1 and z_2 , are then substituted into 4.21 to solve for the reconstructed image, x . For a more complete solution see Appendix B.

The two-step algorithm was implemented in MATLAB, the pseudo-code describes the reconstruction algorithm in MATLAB:

MAP-GMP IMPLEMENTATION:

INITIALIZATION: $x^0 = \text{zeros}(N, N)$,
 $\mu_s = \text{known tissue mean values}$,
 $\sigma_s = \text{estimate standard deviation}$,
 from μ_s and σ_s , estimate initial selection matrix, s^0

LOOP 1: S-STEP: p=1:ITER1

LOOP 2: X-STEP: FOR m=1:ITER2

SOLVE: x^{k+1} from Equations 4.13-4.15

END

LET: $x^0 = x^{k+1}$

ESTIMATE: s^{k+1} from Equation 4.12

END

The results for this algorithm are presented in Section 6.

4.2 Gibbs Sampling

The MAP-GMP algorithm may produce a local minima. To deal with this problem Gibbs Sampling was incorporated into the algorithm. If we let y be the observations, and θ be the parameters, the likelihood of function of y given θ is $p(y|\theta)$. The posterior is:

$$p(\theta|y) = \frac{p(y|\theta)p(\theta)}{p(y)}. \quad (4.17)$$

An alternative estimate to MAP is the posterior mean, given by $E(\theta|y)$:

$$\theta_{CME} = E(\theta|y) = \int_{\theta} \theta p(\theta|y) d\theta, \quad (4.18)$$

using this estimate instead of finding the max of $p(\theta|y)$ we look for a weighted average of the prior mean and the sample mean [10]. Since, $p(\theta|y)$ is unavailable in closed-form, using a Gibbs Sampling approach we draw $p(\theta|y)$ from the observations, $\theta_1, \dots, \theta_L \sim p(\theta|y)$, thus the mean estimate becomes:

$$\tilde{\theta}_{CME} = \frac{1}{L} \sum_{i=1}^L \theta_i, \quad \theta \sim p(\theta|y), \quad (4.19)$$

where L is the number of estimates run. Equation 4.20 shows that the more we iterate, we get samples that are closer to the posterior, hence drawing an average allows the solution to get closer to the mean. The smallest achievable MSE is:

$$MSE(\tilde{\theta}_{CME}) = E\left[(\hat{\theta}_{CME} - \theta)^2\right] \left(1 + \frac{1}{L}\right). \quad (4.20)$$

Gibbs Sampling allows x to be solved for efficiently. With one sample of Gibbs Sampling the MSE is more than twice the mean-square-error (MSE) of the CME estimator.

In the case of image reconstruction, y , are the observations (sinogram), and $\theta = (x, s)$, in order to find the mean estimate, we need to sample x and s from the following distributions:

$$x \sim p(x|s, y), \quad (4.21)$$

$$s \sim p(s|x, y). \quad (4.22)$$

This would be the analytical solution, the iterative solution would be as follows:

$$x^{k+1} \sim p(x|s^k, y), \quad (4.23)$$

$$s^{k+1} \sim p(s|x^k, y). \quad (4.24)$$

where, x would be sampled using the previous estimate of s , and s would be sampled using the previous estimate of x . Equation 4.25 can be re-written as:

$$p(x|s, y) = \frac{p(y, x, s)}{p(y, s)} = \frac{p(y|x)p(x|s)p(s)}{\int p(y|x)p(x|s)p(s)dx}. \quad (4.25)$$

Simplifying 4.25, we determine $p(x|s, y)$ to be a Gaussian distribution with the following mean ($\mu_{x|s, y}$) and variance ($C_{x|s, y}$):

$$\mu_{x|s, y} = \left(\frac{H^T H}{\sigma_x^2} + D \right)^{-1}, \quad (4.26)$$

$$C_{x|s, y} = \left(\frac{H^T H}{\sigma_x^2} + D \right)^{-1} \left(\frac{H^T y}{\sigma_x^2} + D\mu_s \right). \quad (4.27)$$

The solution for x , results in the same solution as in the two-step MAP-GMP algorithm, with the exception of some added noise to y and μ_s :

$$x^{k+1} = x^k + \frac{1}{c} \left(\left(\frac{H^T (y + n_1)}{\sigma_x^2} + D(\mu_s + n_2) \right) - \left(\frac{H^T H}{\sigma_x^2} + D \right) x^k \right). \quad (4.28)$$

The added noise n_1 and n_2 have the following distributions: $n_1 \sim N(0, \sigma_x^2 I_{N \times N})$ and

$$n_2 \sim N \left(0, \text{diag} \begin{pmatrix} \sigma_{s_1}^2 & \cdots & 0 \\ \vdots & \ddots & \vdots \\ 0 & \cdots & \sigma_{s_N}^2 \end{pmatrix} \right). \quad \text{This is incorporated into the MAP solution and}$$

x is drawn from $p(x|s, y)$. The same can be said for sampling s from $p(s|x, y)$:

$$p(s|x, y) = \frac{p(y, x, s)}{p(x, y)} = \frac{p(y|x)p(x|s)p(s)}{\sum_{s_1, \dots, s_N} p(y|x)p(x|s)p(s)dx}. \quad (4.29)$$

Simplifying 4.30 yields the following:

$$P(s_i = s) = c e^{Q_i(s)}, \quad Q_i = \frac{\log(\sigma_s^2)}{2} + \frac{(x_i - \mu_s)^2}{2\sigma_s^2} - \log a_s \quad (4.30)$$

$$c = \left(\sum_{s=1}^S e^{Q_i} \right)^{-1}. \quad (4.31)$$

Where the constant c is chosen so that the $P(s_i = s)$'s sum to one. The value of s_i is drawn from $P(s_i = s)$ for $s_i = 1, 2, \dots, S$. Gibbs Sampling was implemented in MATLAB, the following pseudo-code describes the reconstruction algorithm in MATLAB:

GIBBS IMPLEMENTATION:

INITIALIZATION: $x^0 = \text{zeros}(N, N)$,
 $\mu_s = \text{known tissue mean values}$,
 $\sigma_s = \text{estimate standard deviation}$,
 from μ_s and σ_s , estimate initial selection matrix, s^0

LOOP 1: GIBBS STEP: t=1:ITER1

LOOP 2: S-STEP: p=1:ITER2

LOOP 3: X-STEP: FOR m=1:ITER3

NOISE: Incorporate noise to y , x^k and μ_s

SAMPLE: x^{k+1} given s^k , y , using Equation 4.29

END

LET: $x^0 = x^{k+1}$

SAMPLE: s^{k+1} given x^{k+1} , y , using Equation 4.31

END

$x^0 = x^{k+1}$

$X_{ALL}(:, :, p) = x^{k+1}$

END

$x_{final} = \text{mean}(X_{ALL})$.

5 Simulations

5.1 Image Reconstruction Framework

A Shepp-Logan Phantom and a real x-ray CT Heart Image were used to test the different algorithms mentioned in section 4: unregularized ML, regularized ML, MAP-GMP and Gibbs Sampling. The two images used and the simulation set-up for each of the algorithms are described in the sections that follow.

5.1.1 Shepp Logan Phantom

All of the algorithms were tested using a 128x128 2-D Shepp-Logan phantom that was generated in MATLAB, shown in Figure 5.1, the attenuation values of the pixels are shown in the colorbar on the right of the image and is in .

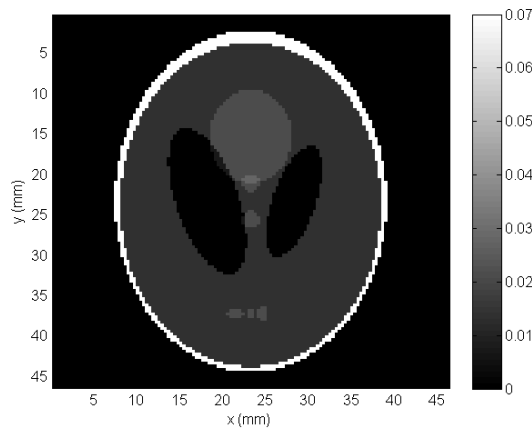


Figure 5.1: 128x128 Shepp Logan Phantom

The Shepp-Logan Phantom is widely used to test and present the quality of reconstruction algorithms. The phantom contains six discrete tissue values and is an ideal representation of some of the different tissues found in the human body. A CT scanner typically returns attenuation values of 0-0.07 hence the Shepp-Logan phantom created was scaled to this range. The size of the phantom was limited to 128x128 due to size constraints in MATLAB. After generating and scaling the phantom, the radon-

transform (or sinogram) of the phantom was found. The sinogram was then used to estimate the original image using each of the algorithms described in Section 4. The algorithms were tested with sinograms containing additive zero-mean Gaussian noise with the noise variances in Table 5.1. The SNR of the noisy sinogram in relation to the original sinogram was calculated as follows:

$$SNR_{ORIGINAL} = 10 \log_{10} \frac{\sum_{t=0}^L \sum_{\theta=0}^M P_{\theta}(t)^2}{\sigma_n^2}, \quad (5.1)$$

where, $P_{\theta}(t)$ is the original sinogram.

Table 5.1: Variance of the noise added to the sinograms in the simulations.

σ_n^2	Shepp $SNR_{ORIGINAL}$ (dB)	CT Image $SNR_{ORIGINAL}$ (dB)
0.000001	46.6008	54.7846
0.000005	39.6124	47.7950
0.00001	36.6013	44.7851
0.00005	29.6165	37.7956
0.0001	26.6163	34.7875
0.0005	19.6533	27.7986
0.001	16.6781	24.7970
0.005	10.0510	17.8692
0.01	7.4858	14.9393

These SNR values in relation to the original image are shown in Table 5.1, notice that as the noise on the added sinogram increases, the $SNR_{ORIGINAL}$ decreases.

The sinogram of the Shepp Logan phantom was generated using 60 projections, at angles varying from $0^\circ - 180^\circ$, with a 3° increase.

5.1.2 Real CT Image

A real CT image of the heart (courtesy of [12]) was used to test the performance of each algorithm (Figure 5.2), this image is 512×512 , due to size constraints in MATLAB this image is too large to use in our algorithms, hence only a portion of it was reconstructed, see Figure 5.3.



Figure 5.2: 512x512 CT Scan of the human heart (From [4]).

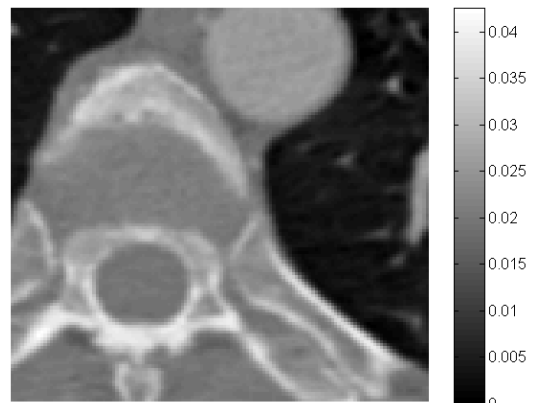


Figure 5.3: 128x128 portion of the human heart. A vertebrae and part of the aorta can be seen in the image.

This CT image had been previously reconstructed (using an unknown technique) and comes in the form of a dicom file (.dcm) with all of the pixels corresponding to a certain tissue (attenuation value) measured in Hounsfield units. The dicom file has information about the type of scanner that was used in the acquisition process, the number of pixels in the image, the pixel range, etc. Since this is a reconstructed image and not the sinogram data itself, the image already contains noise and image artifacts present in the majority of reconstructed CT images. The tissues in this image are not very uniform and in some portions there seems to be a blur or smoothing effect on the image. Using our forward operator, the sinogram for this image was found and the algorithms were tested with sinograms containing additive zero-mean Gaussian noise with the noise variances in Table 5.1 above, just as was done with the Shepp Logan Phantom.

The sinogram of x-ray CT Heart image was generated using 60 projections, at angles varying from $0^\circ - 180^\circ$, with a 3° increase.

5.2 Unregularized Maximum Likelihood

The Maximum Likelihood (ML) algorithm for both the Shepp Logan Phantom and the heart CT image was initialized using an image of all zeros and was run for 1000 iterations. The number of iterations ML was run was chosen by looking at the error and evaluating if it had converged. This algorithm was run with the 18 different sinograms containing added noise of the Shepp Logan Phantom and the x-ray CT heart image (listed in Table 5.1).

For each of the reconstructed images the signal-to-noise ratio (SNR) was calculated by taking the ratio of the expected value of the original image squared and the mean-square-error:

$$SNR_{RECONSTRUCTED} = 10 \log_{10} \frac{E(X^2)}{MSE}, \quad (10.1)$$

$$SNR_{RECONSTRUCTED} = 10 \log_{10} \frac{\sum_{x=0}^{N-1} \sum_{y=0}^{N-1} f(x, y)^2}{\sum_{x=0}^{N-1} \sum_{y=0}^{N-1} (f(x, y) - \hat{f}(x, y))^2}, \quad (10.2)$$

where, $f(x, y)$ is the original image, $\hat{f}(x, y)$ the reconstructed image and N is the dimension of the image [11].

For each of the different sinograms, the algorithm was run ten times. The average, standard deviation, and variance of the ten sets were calculated, and the SNR vs. σ_n^2 was plotted with its corresponding error bars.

5.3 Regularized Maximum Likelihood

Due to the noise being amplified, a regularization term was added to the maximum likelihood algorithm. The error for the regularized ML converged in 100 iterations;

hence the algorithm was run for 100 iterations. The regularized ML was first run letting $\lambda \rightarrow 0$ where $\lambda = \frac{\sigma_n^2}{\sigma_x^2}$ hence, σ_x^2 was taken to be very large in the simulations. Next the regularized ML was run using an optimal value of λ which was found by varying σ_x from 0.001-0.1 and finding the optimal value of σ_x . The optimal value of σ_x for each of the different noisy sinograms is listed in the table below:

Table 5.2: Optimal Values for σ_x for the R-ML for both the Shepp Logan and CT Heart Image

σ_n^2	Shepp σ_x Optimal	CT Image σ_x Optimal
0.000001	0.003	0.003
0.000005	0.006	0.002
0.00001	0.006	0.003
0.00005	0.01	0.003
0.0001	0.01	0.004
0.0005	0.02	0.006
0.001	0.02	0.006
0.005	0.03	0.01
0.01	0.03	0.01

The algorithm was run ten times for each of the different noisy sinograms and for the two cases of λ , $\lambda \rightarrow 0$ and $\lambda_{optimal}$. For each case, the average, standard deviation and variance of each of the ten sets was calculated and the SNR vs. σ_n^2 was plotted with its corresponding error bars.

5.4 MAP with Gaussian Mixture Prior

For the Maximum a Posteriori with a Gaussian Mixture Prior (MAP-GMP), the algorithm involves two steps, the calculation of the x-step and the calculation of the s-step. The x-step and the s-step were run for 100 iterations each; this was chosen by

evaluating the convergence of the error. Since the Shepp-Logan phantom has six different tissues, the mean (μ_s) for the Gaussian functions were chosen to be the values of these tissues see Table 5.3. The optimal standard deviation for the Gaussian functions σ_s was found and used throughout the simulations, Table 5.3 shows μ_s and $\sigma_{s_{optimal}}$.

Table 5.3: Optimal μ_s and σ_s values for the Shepp Logan Phantom using MAP-GMP Reconstruction

Shepp μ_s	Shepp $\sigma_{s_{optimal}}$
0	0.0012639
0.007	0.0012639
0.014	0.0012639
0.021	0.0012639
0.028	0.0012639
0.07	0.0075832

For the Shepp Logan Phantom the optimal σ_s was first fixed as $\sigma_s = \sqrt{\mu_s - \mu_{s+1}}$ for $s = \{1 \ 2 \dots 6\}$ and then reducing it by 1% until a reconstructed image with the highest SNR was found.

The mean and variance values for the CT heart image were found by plotting a histogram of the image shown in blue, in Figure 5.4, and centering a Gaussian distribution around the main histogram distributions shown in red, in Figure 5.4. The optimal σ_s was found by first allowing σ_s to be very large and reducing it by 1% until the reconstructed image with the highest SNR was found. The mean tissue value and σ_s are shown in Table 5.4.

Table 5.4: Optimal λ and μ values for the Heart CT Image using MAP-GMP Reconstruction

CT Image	CT Image
0	0.000613
0.01	0.0019
0.0181	0.0019
0.0202	0.0021
0.0256	0.0027

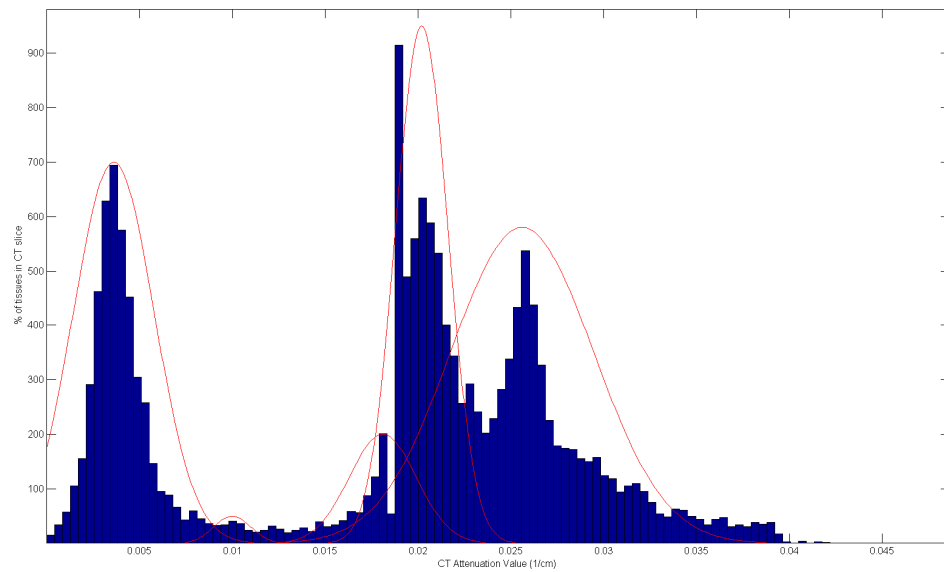


Figure 5.4: Histogram of the CT Heart Image with Gaussian Distributions

For both the Shepp Logan Phantom and the CT heart image a certain weight known as w_i was given to each of the different Gaussian functions; for this simulation all tissues were given the same weight of $w_i = 1$. In order to find an initial estimate of μ_i , where μ_i the original image was used.

With $I(S_i = s)$, each of the pixels in the image is assigned to a certain tissue, and $\mu(S_i = s)$ and $\sigma_s^2(S_i = s)$ are found as well. Random noise between the values of 0-0.007 was then added to $\mu(S_i = s)$, since in the real world we would not have the original image, only the poor or noisy estimate of the reconstruction. For the x-step the algorithm was initialized with an image of all zeros.

MAP-GMP was run for each of the noisy sinograms, 10 times, with new noise being generated every time it was run. The average, standard deviation, and variance of each of the ten sets was calculated, and the SNR vs. σ_n^2 was plotted with its corresponding error bars.

5.5 Gibbs Sampling Prior

For the Gibbs Reconstruction Algorithm (GRA), $I(S_i = s)$, $\mu(S_i = s)$ and $\sigma_s^2(S_i = s)$ were initialized and found in the same way as the MAP-GM algorithm along with the optimal σ_s . The optimal standard deviation σ_s found and used throughout the simulations for the Shepp Logan Phantom and the CT Image are summarized in Table 5.5 and Table 5.6.

Table 5.5: Optimal σ_s values for the Gibbs Reconstruction for the Shepp Logan Phantom.

Shepp μ_s	Shepp $\sigma_{s_{optimal}}$
0	0.0010664
0.007	0.0010664
0.014	0.0010664
0.021	0.0010664
0.028	0.0010664
0.07	0.0063987

Table 5.6: Optimal σ_s values for the Gibbs Reconstruction for the Heart CT Image

CT Image μ_s	CT Image $\sigma_{s\text{optimal}}$
0.00362	0.000682
0.01	0.0021
0.0181	0.0021
0.0202	0.0024
0.0256	0.003

The weight assigned to each of the Gaussian functions for the Shepp Logan phantom, a_s was also set to 1/6 as in the MAP-GMP algorithm and for the heart image $a_s = \frac{1}{5}$. Since there are three steps to the GRA, the x-step, the s-step and the Gibbs-step, the number of iterations used for the x-step and the s-step were each set to 20 iterations and the Gibbs-step was set to run for 10 iterations for both images. The x and s-step were set to 20 because the error at that point had converged. For the Gibbs-step 10 iterations were chosen because it gave a fair reconstruction of the image. The higher the iterations for the Gibbs step, the higher the SNR of the reconstructed image but the reconstruction takes a long time to perform so the iterations were limited to 10. The GRA was run for each of the noisy sinograms, 10 times, with new noise being generated every time it was run. The average, standard deviation and variance of each of the ten sets was calculated and the SNR vs. σ_n^2 was plotted with its corresponding error bars.

6 Results

6.1 Shepp Logan Phantom

The $\text{SNR}_{\text{RECONSTRUCTED}}$ versus $\text{SNR}_{\text{ORIGINAL}}$ for all five reconstruction techniques were plotted against each other and are depicted in Figure 6.1. As can be seen from the graph, MAP-GMP and Gibbs perform better than the unregularized and regularized ML.

When the noise level on the sinogram is low, $\text{SNR}_{\text{ORIGINAL}} \approx 47\text{dB}$, the regularized and unregularized ML perform the same since the noise is very small and that is the maximum amount of information ML can obtain from the projection data. The Gibbs reconstruction performed 17dB better than the MAP-GMP reconstruction at this noise level; MAP needs more information about the image in order to obtain a reconstructed image with a higher SNR, whereas Gibbs does not need as much information since it samples from the posterior.

With the highest noise added to the sinogram, $\text{SNR}_{\text{ORIGINAL}} \approx 7.5\text{dB}$, the optimal regularized ML, MAP-GMP and Gibbs performed the same. At this point the Gaussian Mixture Prior needed for the MAP and Gibbs reconstruction is really wide and uniform (σ_s^2 is large) matching the regularization prior added to the ML reconstruction; hence they obtain the same results.

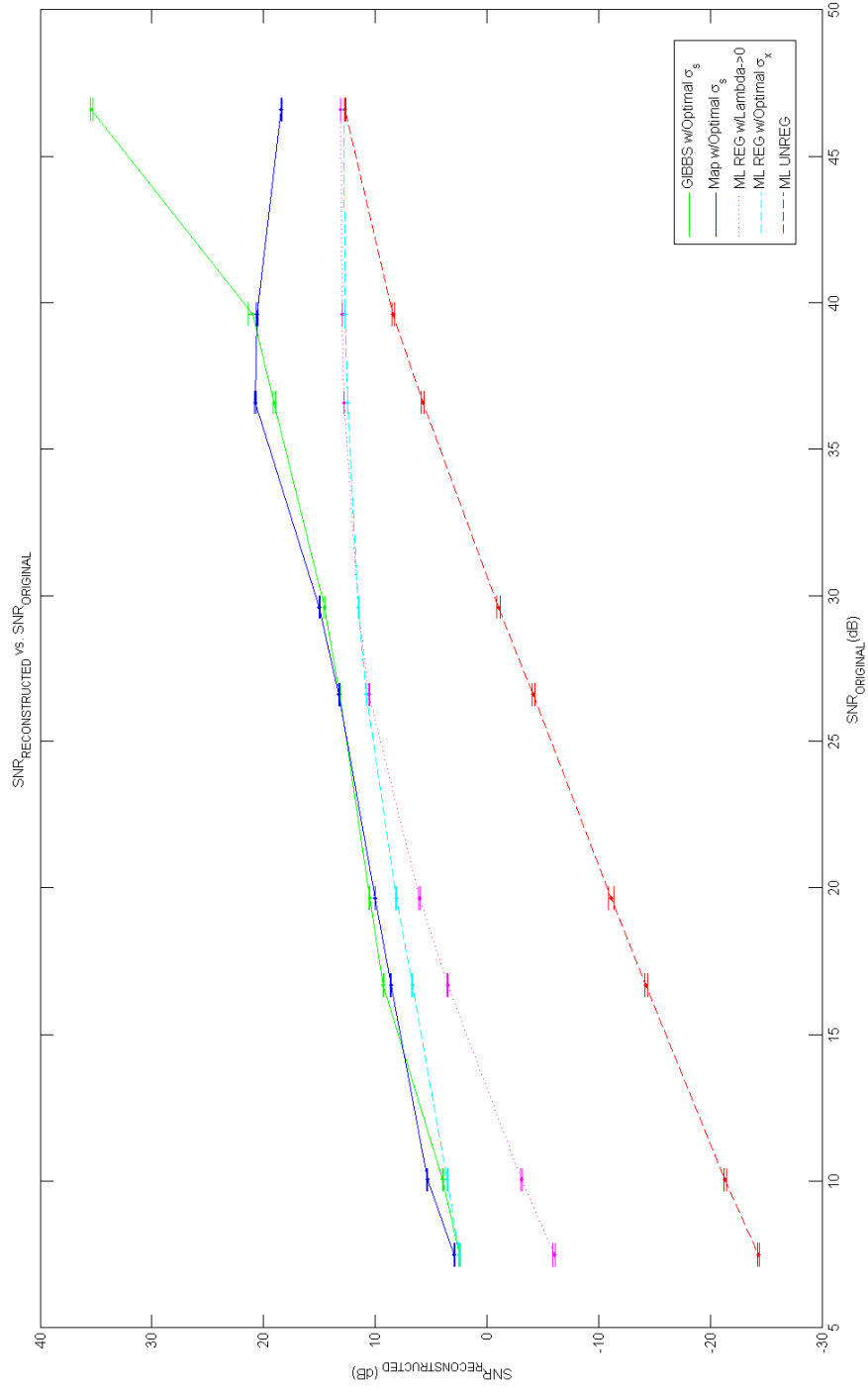


Figure 6.1: SNR_{RECONSTRUCTED} vs. SNR_{ORIGINAL} for the Shepp Logan Phantom, using 5 different methods.

Between $\text{SNR}_{\text{ORIGINAL}}$ of 5-40dB, Gibbs Sampling and MAP-GMP perform relatively the same. This is due to the fact that Gibbs Sampling gets stuck on the initial tissue the pixel has been estimated to be and requires many more iterations in order for a pixel to switch from one tissue to the next, especially if the priors for those tissues are far from one another. For example if pixel (1,1) is of Tissue #1, but it was initially estimated as being Tissue #3, it may take a long time (a lot of iterations) for this tissue to switch to Tissue #1. This phenomena is shown in the two reconstructed images of the Shepp Logan phantom in Figure 6.2 and Figure 6.3. These were reconstructed using $\sigma_{s_i}^2 = 0.007$ for all tissues $i = \{1, 2 \dots, 6\}$. The image on the right has been run for 10 Gibbs Sampling iterations whereas the image on the left for 10,000 Gibbs Sampling iterations, if you look at the pixels with intensity of 0.065-0.07 at the upper portion of the phantom, most of the pixels are of intensity 0.04-0.05, and it took 10,000 Gibbs Sampling iterations for some of those pixels to begin switching over to their correct value of 0.07.

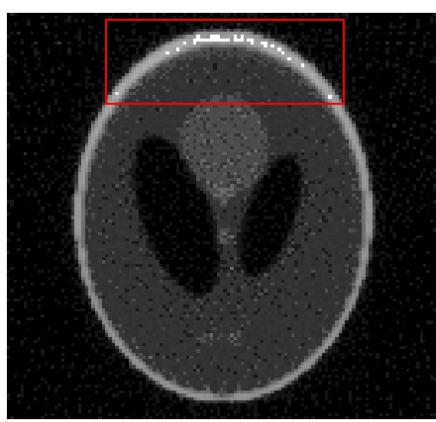


Figure 6.2: Gibbs Sampling Reconstruction, 10 iterations

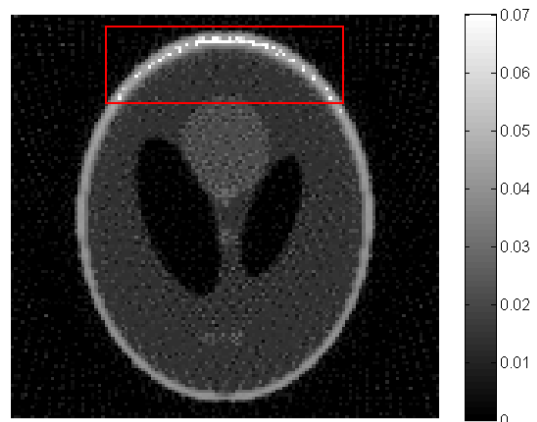


Figure 6.3: Gibbs Sampling Reconstruction, 1000 iterations

Several images are presented in Figure 6.4 - Figure 6.18 for a $\text{SNR}_{\text{ORIGINAL}}$ of 46.6 dB, 26.6 dB and 7.4958 dB. For the unregularized ML, the more iterations it is run, the more the image begins to degenerate, as seen in Figure 6.1. Unregularized ML significantly overestimates the values of the image, causing the SNR to decrease. As

can be seen in image Figure 6.18, ML introduces a checkerboard effect where all the pixels have very high or low values. For this reason a regularization term was added that controlled the overestimation of pixel intensities. If the $\text{SNR}_{\text{ORIGINAL}}$ is less than 25dB, R-ML begins to act like U-ML and degenerates the image as the iterations increase. When a large amount of noise is added, R-ML does not have enough information to reconstruct the image properly, λ becomes approximately 0 and the regularization term begins to have little to no effect on the reconstruction, making it unstable like U-ML.

As can be seen in the images presented in Figure 6.4 - Figure 6.18, as the noise on the sinogram increases, a good quality reconstruction becomes increasingly difficult to estimate. Looking at Figures 6.4 – Figure 6.8, the Gibbs Sampling algorithm was able to reconstruct an image almost identical to the original image, the reconstruction with MAP-GMP had slight reconstruction artifacts around the head of the Shepp-Logan Phantom, while the regularized and unregularized ML had a increase in artifacts all over the image.

Figure 6.9 - Figure 6.13, contain a noise $\text{SNR}_{\text{ORIGINAL}}$ of 26.6 dB, at this increased SNR Gibbs Sampling and MAP-GMP performed the same, with MAP-GMP having a slightly better $\text{SNR}_{\text{RECONSTRUCTED}}$ of 0.05 dB. At this $\text{SNR}_{\text{RECONSTRUCTED}}$ the Gibbs Sampling reconstructed image looks sharper than the MAP-GMP, but the MAP-GMP contains more uniform tissue (pixel) values. Both of the regularized ML performed worse than Gibbs Sampling and MAP-GMP hence the image contains more artifacts. The unregularized case performed worse than all other methods, overestimating all tissue values.

Figure 6.14-Figure 4.18, demonstrate the reconstructed images with the highest amount of noise added to the sinogram $\text{SNR}_{\text{ORIGINAL}}$ of 7.5 dB. At these noise level Gibbs Sampling, MAP-GMP and regularized ML with λ_{optimal} performed the same, but the images look significantly different. Gibbs Sampling and MAP-GMP were able to estimate more accurately the tissue values at an attenuation value of 0 and 0.07,

but were not able to reconstruct anything inside the Shepp Logan Phantom head. Regularized ML was able to estimate more of the pixels inside the Shepp Logan Phantom head but the pixel values were overestimated and the image appears with an increase in artifacts. For the unregularized ML the pixel values were overestimated significantly and a checkerboard effect is seen.



Figure 6.4: Gibbs Sampling, optimal σ_S . $\text{SNR}_{\text{ORIGINAL}} = 46.6$ dB, $\text{SNR}_{\text{RECONSTRUCTED}} = 35.3069$ dB



Figure 6.5: MAP Reconstruction, optimal σ_S . $\text{SNR}_{\text{ORIGINAL}} = 46.6$ dB, $\text{SNR}_{\text{RECONSTRUCTED}} = 18.3595$ dB

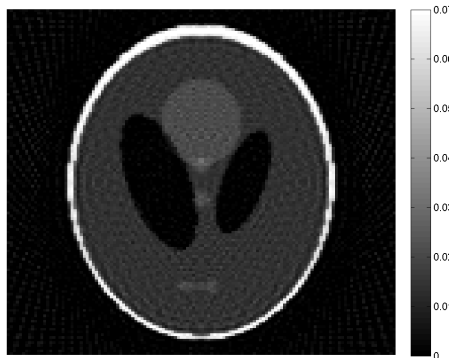


Figure 6.6: Regularized ML, $\lambda \rightarrow 0$, $\text{SNR}_{\text{ORIGINAL}} = 46.6$ dB, $\text{SNR}_{\text{RECONSTRUCTED}} = 12.8479$ dB

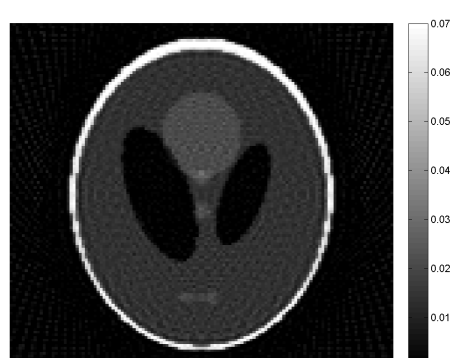


Figure 6.7: Regularized ML, λ_{opt} , $\text{SNR}_{\text{ORIGINAL}} = 46.6$ dB, $\text{SNR}_{\text{RECONSTRUCTED}} = 13.0463$ dB

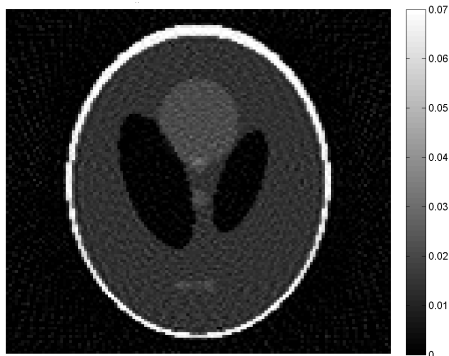


Figure 6.8: Unregularized ML, $\text{SNR}_{\text{ORIGINAL}} = 46.6$ dB, $\text{SNR}_{\text{RECONSTRUCTED}} = 12.6784$ dB

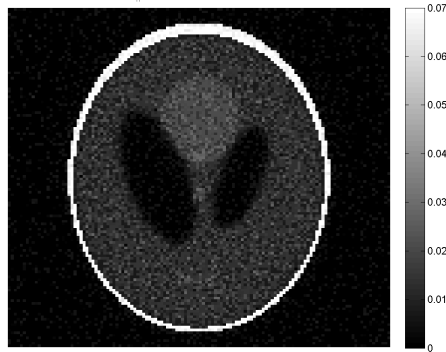


Figure 6.9: Gibbs Sampling, optimal σ_S . $\text{SNR}_{\text{ORIGINAL}}=26.6$ dB, $\text{SNR}_{\text{RECONSTRUCTED}} = 13.2021$ dB

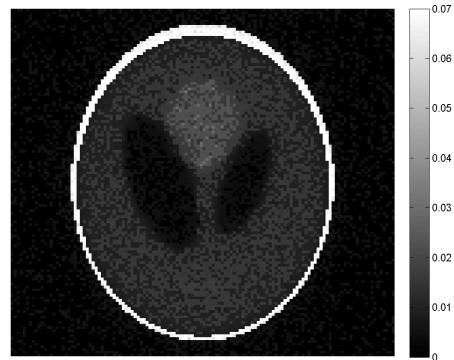


Figure 6.10: MAP Reconstruction, optimal σ_S . $\text{SNR}_{\text{ORIGINAL}}= 26.6$ dB, $\text{SNR}_{\text{RECONSTRUCTED}} = 13.225$ dB

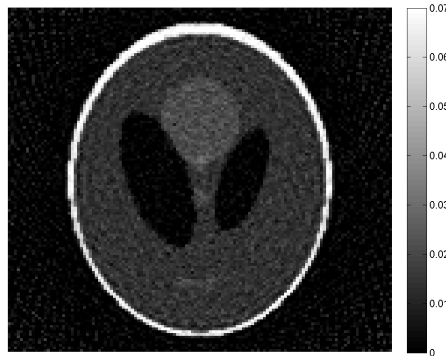


Figure 6.11: Regularized ML, $\lambda \rightarrow 0$, $\text{SNR}_{\text{ORIGINAL}}= 26.6$ dB, $\text{SNR}_{\text{RECONSTRUCTED}} = 10.401$ dB

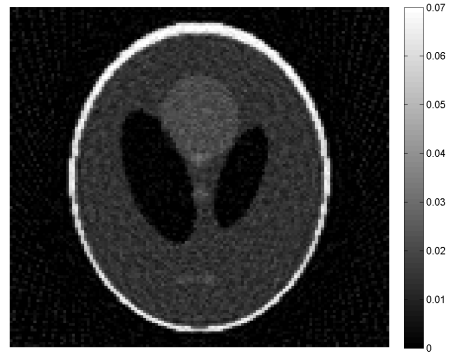


Figure 6.12: Regularized ML, λ_{opt} , $\text{SNR}_{\text{ORIGINAL}}= 26.6$ dB, $\text{SNR}_{\text{RECONSTRUCTED}} = 11.3646$ dB

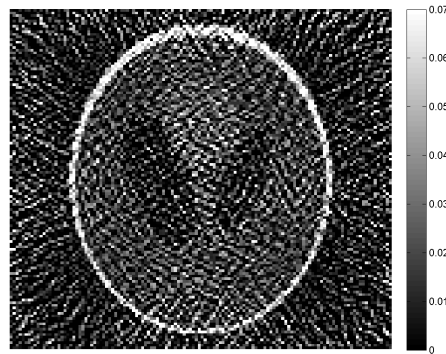


Figure 6.13: Unregularized ML, $\text{SNR}_{\text{ORIGINAL}}= 26.6$ dB, $\text{SNR}_{\text{RECONSTRUCTED}} = -4.1653$ dB

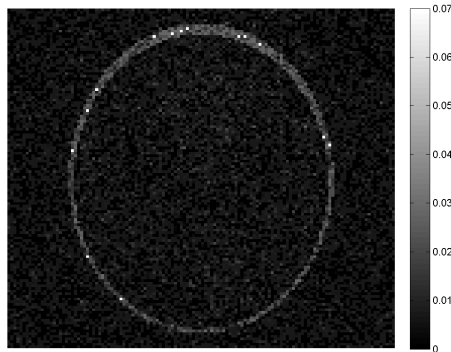


Figure 6.14: Gibbs Sampling, optimal σ_S . $\text{SNR}_{\text{ORIGINAL}} = 7.5$ dB,
 $\text{SNR}_{\text{RECONSTRUCTED}} = 2.4363$ dB

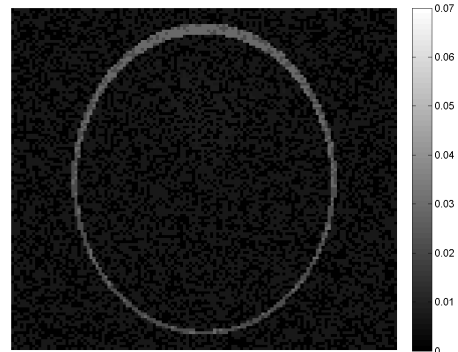


Figure 6.15: MAP Reconstruction, optimal σ_S . $\text{SNR}_{\text{ORIGINAL}} = 7.5$ dB,
 $\text{SNR}_{\text{RECONSTRUCTED}} = 2.8989$ dB

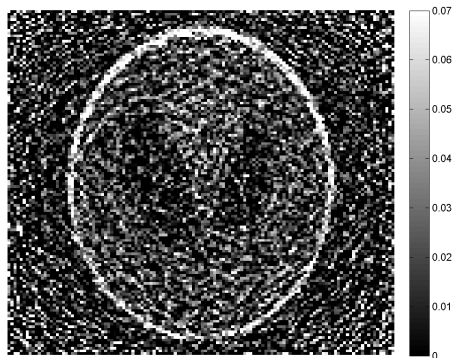


Figure 6.16: Regularized ML, $\lambda \rightarrow 0$, $\text{SNR}_{\text{ORIGINAL}} = 7.5$ dB,
 $\text{SNR}_{\text{RECONSTRUCTED}} = 0.86642$ dB

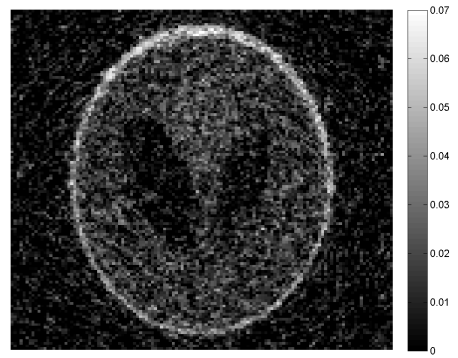


Figure 6.17: Regularized ML, λ_{opt} , $\text{SNR}_{\text{ORIGINAL}} = 7.5$ dB,
 $\text{SNR}_{\text{RECONSTRUCTED}} = 2.9225$ dB

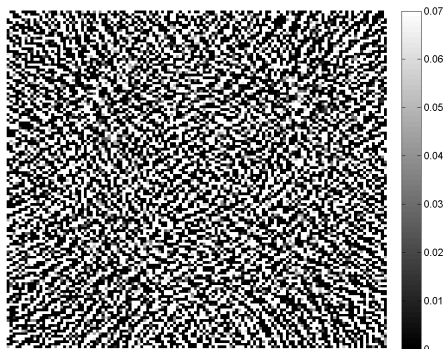


Figure 6.18: Unregularized ML, $\text{SNR}_{\text{ORIGINAL}} = 7.5$ dB,
 $\text{SNR}_{\text{RECONSTRUCTED}} = -24.2185$ dB

6.2 Real CT Image

For the real CT image of the heart, the $\text{SNR}_{\text{RECONSTRUCTED}}$ versus $\text{SNR}_{\text{ORIGINAL}}$ was plotted and is shown in Figure 6.19. Also, several images are presented in Figure 6.20 - Figure 6.34 for a $\text{SNR}_{\text{ORIGINAL}}$ of 54.8 dB, 34.8 dB and 14.9 dB. With the heart image, the regularized ML using λ_{opt} outperformed all of the other reconstruction methods when $\text{SNR}_{\text{ORIGINAL}}$ was above 25 dB, including Gibbs Sampling and the MAP-GMP reconstructions. Even when there was very little noise it tended to perform ~ 6 dB greater than MAP-GMP and ~ 10 dB greater than Gibbs. From these results we see that Gibbs Sampling and MAP-GMP are highly dependent on the chosen values for σ_s , a more optimal value than the one found for σ_s may yield better results.

The low SNR values for the Gibbs Sampling and MAP-GMP may also be due to the fact that the current image already has noise, so tissues which should be uniform are not. The type of noise that ML adds to the image may be more comparable to the noise that is already currently on the CT image of the heart. For example, looking at Figure 6.21 and Figure 6.23, for MAP-GMP and regularized ML using λ_{opt} , respectively, you see that the pixels in the image of the MAP-GMP reconstruction are much more uniform in value; there are also some pixels that are trapped in a local minima. Now looking at the regularized ML using λ_{opt} , you see there are some reconstruction errors in the image; to the left of the image you see some projection artifacts that fan out of the image and the tissues are much less uniform; there is also a smoothing effect between tissue transitions.

It is interesting to note that at $\text{SNR}_{\text{ORIGINAL}} \approx 15$ dB Gibbs Sampling performed only 2 dB less than the regularized ML using λ_{opt} and MAP-GMP performed ~ 9 dB less. Gibbs Sampling outperformed MAP-GMP in this case because Gibbs Sampling gives

equal probability to all of the possible values of, s_i , whereas MAP-GMP chooses only the minimum values of s_i .

The unregularized ML performed as expected, attaining very low SNR for all reconstructions of the image compared to the other algorithms.

As can be seen in the images presented in Figure 6.20 - Figure 6.34, as the noise on the sinogram increases the quality of the reconstructed image decreases. Figure 6.20 - Figure 6.24, demonstrate the images reconstructed from a sinogram with the least amount of added noise. In this case, the regularized ML performed better than Gibbs Sampling and MAP-GMP, with the regularized ML images appearing to be much smoother than the Gibbs Sampling and MAP-GMP. Unregularized ML produced a grainy image with overestimated tissue values.

For Figure 6.25 – Figure 6.29, $\text{SNR}_{\text{ORIGINAL}}=34.8$ dB, the Gibbs Sampling reconstructed image appears slightly more grainy than the MAP-GMP, MAP-GMP had a better estimation of pixel values, but both methods produces very even tissue values resulting in a sharper looking image. The regularized ML generated images that were much smoother. The unregularized ML completely overestimated all tissue values creating a checkerboard effect of the image.

For Figure 6.25 – Figure 6.29, $\text{SNR}_{\text{ORIGINAL}}=14.9$ dB, the Gibbs Sampling and MAP-GMP were able to generate an image with an outline of the general structures of the image and the images appear pixelized. For the regularized ML with λ_{optimal} the reconstructed image looks very smooth and resulted in a more accurate image. When λ was taken to 0, the pixel values were over estimated and a checkerboard image begins to appear. For the unregularized ML the pixel values were completely overestimated and nothing is able to be seen in the reconstructed image.

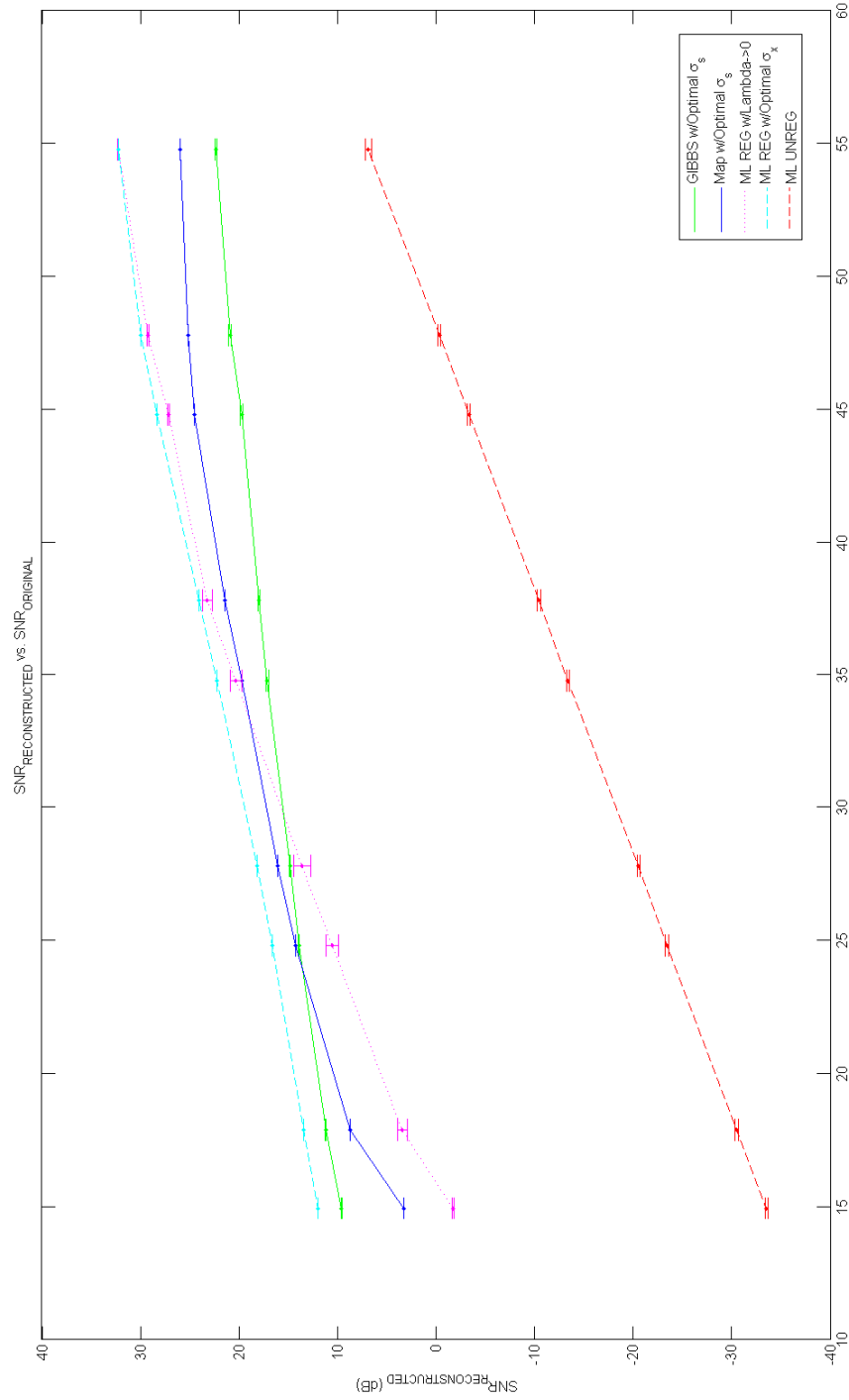


Figure 6.19: SNR_{RECONSTRUCTED} vs. SNR_{ORIGINAL} for the CT Image of the human heart, using 5 different methods.

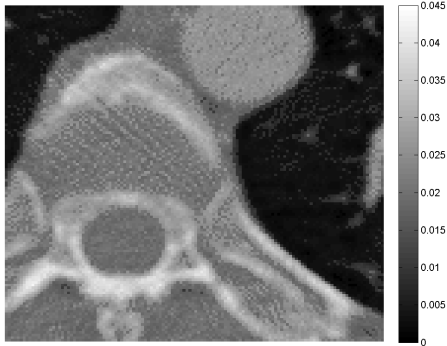


Figure 6.20: Gibbs Sampling, optimal σ_s . $\text{SNR}_{\text{ORIGINAL}} = 54.8 \text{ dB}$,
 $\text{SNR}_{\text{RECONSTRUCTED}} = 22.3419 \text{ dB}$



Figure 6.21: MAP Reconstruction, optimal σ_s . $\text{SNR}_{\text{ORIGINAL}} = 54.8 \text{ dB}$,
 $\text{SNR}_{\text{RECONSTRUCTED}} = 25.9815 \text{ dB}$

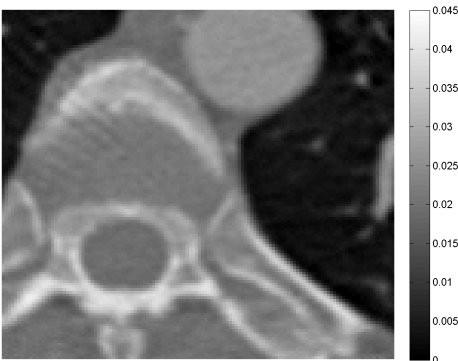


Figure 6.22: Regularized ML, $\lambda \rightarrow 0$,
 $\text{SNR}_{\text{ORIGINAL}} = 54.8 \text{ dB}$,
 $\text{SNR}_{\text{RECONSTRUCTED}} = 32.323 \text{ dB}$



Figure 6.23: Regularized ML, λ_{opt} ,
 $\text{SNR}_{\text{ORIGINAL}} = 54.8 \text{ dB}$,
 $\text{SNR}_{\text{RECONSTRUCTED}} = 32.2658 \text{ dB}$

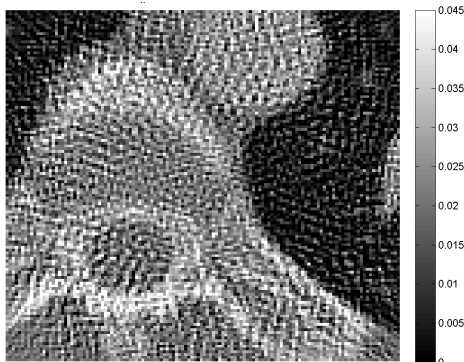


Figure 6.24: Unregularized ML,
 $\text{SNR}_{\text{ORIGINAL}} = 54.8 \text{ dB}$,
 $\text{SNR}_{\text{RECONSTRUCTED}} = 6.4731 \text{ dB}$

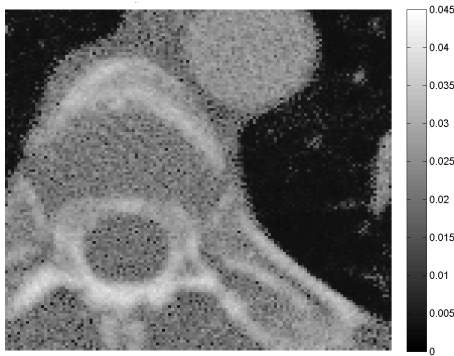


Figure 6.25: Gibbs Sampling, optimal σ_s .
 $\text{SNR}_{\text{ORIGINAL}} = 34.8 \text{ dB}$,
 $\text{SNR}_{\text{RECONSTRUCTED}} = 17.2853 \text{ dB}$

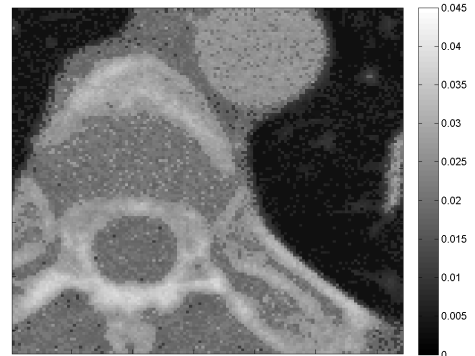


Figure 6.26: MAP Reconstruction, optimal σ_s . $\text{SNR}_{\text{ORIGINAL}} = 34.8 \text{ dB}$,
 $\text{SNR}_{\text{RECONSTRUCTED}} = 19.7247 \text{ dB}$

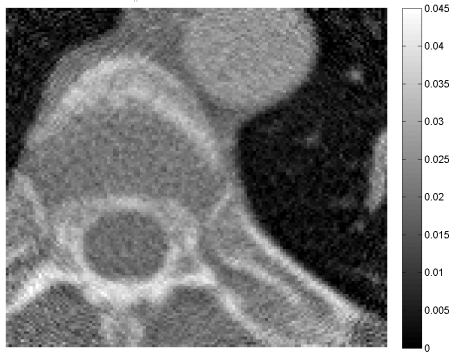


Figure 6.27: Regularized ML, $\lambda \rightarrow 0$,
 $\text{SNR}_{\text{ORIGINAL}} = 34.8 \text{ dB}$,
 $\text{SNR}_{\text{RECONSTRUCTED}} = 20.94 \text{ dB}$

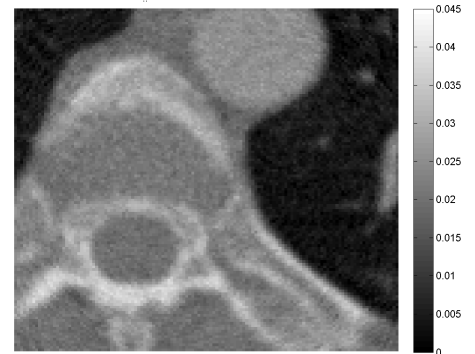


Figure 6.28: Regularized ML, λ_{opt} ,
 $\text{SNR}_{\text{ORIGINAL}} = 34.8 \text{ dB}$,
 $\text{SNR}_{\text{RECONSTRUCTED}} = 22.2201 \text{ dB}$

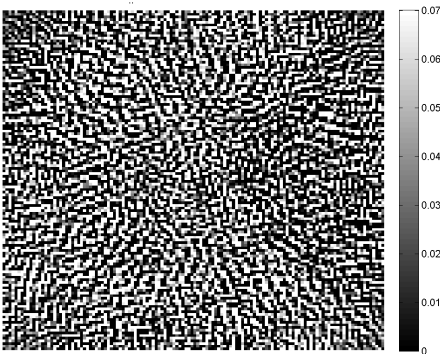


Figure 6.29: Unregularized ML,
 $\text{SNR}_{\text{ORIGINAL}} = 34.8 \text{ dB}$,
 $\text{SNR}_{\text{RECONSTRUCTED}} = -13.5526 \text{ dB}$

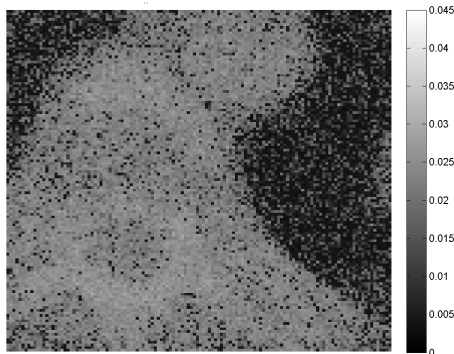


Figure 6.30: Gibbs Sampling, optimal σ_s . $\text{SNR}_{\text{ORIGINAL}} = 14.9$ dB,
 $\text{SNR}_{\text{RECONSTRUCTED}} = 9.5479$ dB

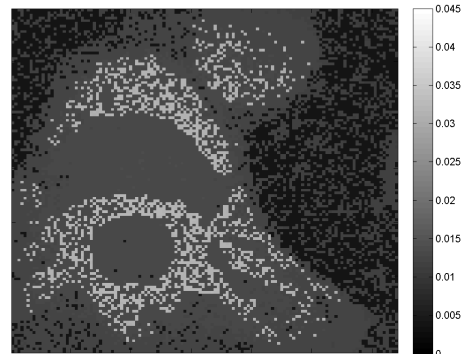


Figure 6.31: MAP Reconstruction, optimal σ_s . $\text{SNR}_{\text{ORIGINAL}} = 14.9$ dB,
 $\text{SNR}_{\text{RECONSTRUCTED}} = 3.2036$ dB

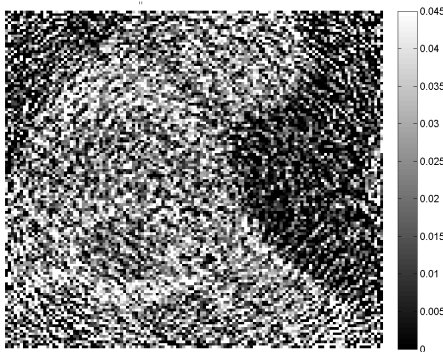


Figure 6.32: Regularized ML, $\lambda \rightarrow 0$,
 $\text{SNR}_{\text{ORIGINAL}} = 14.9$ dB,
 $\text{SNR}_{\text{RECONSTRUCTED}} = -1.7491$ dB

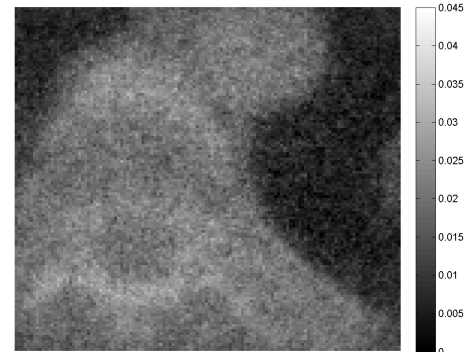


Figure 6.33: Regularized ML, λ_{opt} ,
 $\text{SNR}_{\text{ORIGINAL}} = 14.9$ dB,
 $\text{SNR}_{\text{RECONSTRUCTED}} = 11.9609$ dB

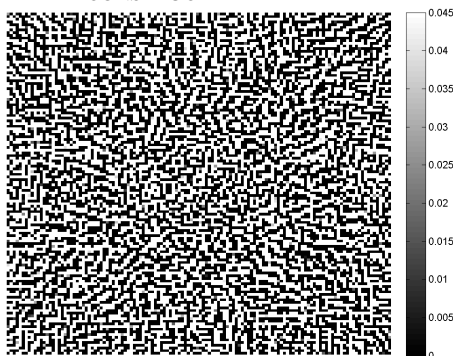


Figure 6.34: Unregularized ML,
 $\text{SNR}_{\text{ORIGINAL}} = 14.9$ dB,
 $\text{SNR}_{\text{RECONSTRUCTED}} = -33.4604$ dB

7 Conclusions

In medicine, early and correct diagnosis of an illness is preferred and necessary. Advance imaging technologies such as CT, MRI, and PET are used daily to save lives; hence, the need and desire to continually improve image reconstruction algorithms. This thesis presented statistical priors to the X-ray CT reconstruction algorithm in an attempt to improve more classical solutions.

Based on the results presented in this thesis, the MAP-GMP and Gibbs Sampling approach are very useful when images have very discrete tissue values. These algorithms resulted in images that have uniform tissue values and a clear separation between tissues. When there is a lot of mixing between tissues these algorithms do not perform optimally. Both techniques exceeded the results of unregularized ML and regularized ML when it came to a uniform image; when it came to an image that had a lot of mixing between tissues regularized ML outperformed all methods.

Image reconstruction is an ongoing field and improved methods are continuously being developed. This thesis describes the development of two image reconstruction approaches: MAP with a Gaussian mixture prior and MAP with Gibbs Sampling, which resulted in improved reconstruction (high SNR) of uniform images compared to classical solutions such as regularized and unregularized maximum likelihood. This first proof of concept can be used to learn the impact of predicting more accurately the presence of certain tissues. These methods can be further explored and improved to attain additional improvement in the reconstructed image, thus providing medical professionals with better images for diagnosis without the patient undergoing additional exposure to radiation.

7.1 Future Work

Several changes can be made to improve MAP-GMP and the Gibbs Sampling approach, such as finding a way to choose a more optimal σ_s and modeling the noise as a Poisson distribution instead of a Gaussian distribution; this will allow MAP-GMP

and Gibbs Sampling to perform better, attaining a higher SNR. In addition, the spatial correlation between pixels can also be incorporated to improve the results by taking advantage of the local similarity of pixels. Also, a histogram with a wider range of gray scale values can also be used to improve the selection of the prior.

Bibliography

- [1] Candes, E., & Romberg, J. (2005). Practical Signal Recovery from Random Projections. *SPIE International Symposium on Electronic Imaging: Computational Imaging III*. San Jose, CA.
- [2] Cevher, V., Duarte, M. F., Hegde, C., & Baraniuk, R. G. (2008, Dec.). Sparse Signal Recovery Using Markov Random Fields. *Proc. Workshop on Neural Info. Proc. Sys. (NIPS)* . Vancouver, Canada.
- [3] De Witte, Y., Vlassenbroeck, J., & Van Hoorebeke, L. (2010). A Multiresolution Approach to Iterative Reconstruction Algorithms in X-Ray Computed Tomography. *IEEE Transactions on Image Processing*.
- [4] Yin, J., Tian, X., Tang, Z., & Sun, Y. (2006). A Histogram-Based Fast Enhancement Algorithm for CT Head Images. *ICBPE 2006. International Conference on Biomedical and Pharmaceutical Engineering*, (pp. 39-43).
- [5] Shung, K. K., Smith, M. B., & Tsui, B. (1992). *Principles of Medical Imaging*. San Diego: Academic Press.
- [6] Buzug, T. M. (2008). *Computed Tomography: From Photon Statistics to Modern Cone-Beam CT*. Leipzig: Springer.
- [7] Kak, A. C., & Slaney, M. (1988). *Principles of Computerized Tomographic Imaging*. New York: IEEE Press.
- [8] Herman, G. T., & Kuba, A. (2003). Discrete Tomography in Medical Imaging. *Proceedings of the IEEE* , 1612-1626.
- [9] Lange, K., Hunter, D. R., & Yang, I. (2000). Optimization Transfer Using Surrogate Objective Functions. *Journal of Computational and Graphical Statistics* , 1-20.
- [10] Awate, S. P. (2007). *Adaptive Nonparametric Markov Models and Information-Theoretic Methods for Image Restoration and Segmentation*. Retrieved September 15, 2009, from http://www.cs.utah.edu/~suyash/Dissertation_html/node81.html
- [11] Gonzalez, R. C., & Woods, R. E. (2008). *Digital Image Processing*. Upper Saddle River: Pearson Education.

- [12] (n.d.). Retrieved May 10, 2010, from DICOM Sample Image Sets: <http://pubimage.hcuge.ch:8080/>
- [13] August, J. (2002). Decoupling the Equations of Regularized Tomography. *IEEE International Symposium on Biomedical Imaging* (pp. 653-656). IEEE.
- [14] Chan, M. T., & Herman, G. T. (1989). Bayesian Image Reconstruction using Image-Modeling Gibbs Priors. *International Journal of Imaging Systems & Technology*, Vol. 9, 85-98.
- [15] Chen, W., & Najarian, K. (2009). Segmentation of Brain CT Images Using Gaussian Mixture Model Method. *Complex Medical Engineering*, 1-6.
- [16] Gardner, R. J., & Gritzmann, P. (1997). Discrete Tomography: Determination of Finite Sets of X-Rays. *Transactions of the American Mathematical Society*, 2271-2295.
- [17] Geman, S., & Geman, D. (1984). Stochastic Relaxation, Gibbs Distributions, and the Bayesian Restoration of Images. *Pattern Analysis and Machine Intelligence, IEEE Transactions*, 721-741.
- [18] Gonzalez, R. C., Woods, R. E., & Eddins, S. L. (2004). *Digital Image Processing Using MATLAB*. Upper Saddle River: Pearson Prentice Hall.
- [19] Higdon, D. M., Bowsher, J. E., Johnson, V. E., Turkington, T. G., Gilland, D. R., & Jaszczak, R. J. (1997). Fully Bayesian Estimation of Gibbs Hyperparameters for Emission Computed tomography Data. *IEEE Transactions on Medical Imaging*, Vol. 16, 516-526.
- [20] Johansson, B., Elfving, T., Kozlov, V., Censor, Y., & Granlund, G. (2006). The Application of an Oblique-Projected Landweber Method to a Model of Supervised Learning. *Mathematical and Computer Modelling*, Vol. 43, 892-909.
- [21] Kontaxakis, G., & Strauss, L. G. (1998). Maximum Likelihood Algorithms for Image Reconstruction in Positron Emission Tomography.
- [22] Lei, T., & Sewchand, W. (1992). Statistical Approach to X-Ray CT Imaging and Its Applications in Image Analysis-Part II: A New Stochastic Model-Based Image Segmentation Technique for X-Ray CT Image. *IEEE Transactions on Medical Imaging Vol. 11*, 62-69.

- [23] Lei, T., & Wilfred, S. (1992). Statistical Approach to X-Ray CT Imaging and Its Applications in Image Analysis-Part I: Statistical Analysis of X-Ray CT Imaging. *IEEE Transactions on Medical Imaging*, Vol. 11, 53-61.
- [24] Mantala, C., & Theera-Umpon, N. (2006). X-Ray Computed Tomography for Metals Using Fourier Reconstruction. *IECON 2006, 32nd Annual IEEE Industrial Electronics Conference*, (pp. 5463-5467). Paris.
- [25] Myers, G. R., Thomas, D. C., Paganin, D. M., Gureyev, T. E., & Clement, J. G. (2010). A General Few-Projection Method for Tomographic Reconstruction of Samples Consisting of Several Distinct Materials. *Applied Physics Letters*, 021105 - 021105-3.
- [26] Ollinger, J. M. (1994). Maximum-Likelihood Reconstruction of Transmission images in Emission Computed Tomography via the EM Algorithm. *IEEE Transactions on Medical Imaging*, Vol. 13, 89-101.
- [27] Rifkin, R. M., & Lippert, R. A. (2007). *Notes on Regularized Least Squares*. Cambridge: CSAIL.
- [28] Shi, J., & Malik, J. (2000). Normalized Cuts and Image Segmentation. *IEEE Transactions on Pattern Analysis and Machine Intelligence*, Vol. 22, 888-905.
- [29] Wainwright, M. J., Ravikumar, P., & Lafferty, J. D. (2007). High Dimensional Graphical Model Selection using l_1 -Regularized Logistic Regression. *Advances in Neural Information Processing Systems 19*, 1465-1472.
- [30] Zhou, Z., Leahy, R. M., & Qi, J. (1997). Aproximate Maximum Likelihood Hyperparameter Estimation for Gibbs Priors. *IEEE Transacations on Image Processing*, Vol. 6, 844-861.

Appendices

Appendix A – Maximum Likelihood

A.1 Unregularized Maximum Likelihood

In Maximum Likelihood we model y as being a Gaussian distribution where the mean is Hx , and standard deviation is σ_n^2 , $y \sim N(Hx, \sigma_n^2 I)$, and the cost function can be defined as:

$$p(y|x) = \frac{1}{(\sqrt{2\pi\sigma_n^2})^m} e^{-\frac{\|y-Hx\|^2}{2\sigma_n^2}}, \quad (1.1)$$

where, y is the projection data (this images is known as the sinogram), H is the forward operator (radon transform of x), and σ_n the standard deviation of the noise on y . The negative log likelihood function of the above equation simplifies to:

$$\begin{aligned} L(p) &= -\log(p(y|x)p(x)) \\ &= \frac{\|y - Hx^{k+1}\|^2}{2\sigma_n^2} + \frac{m}{2} \log(2\pi\sigma_n^2). \end{aligned} \quad (1.2)$$

Expanding Equation 3.7 results in the following:

$$\begin{aligned} L(p) &= \frac{1}{2\sigma_n^2} (\|y - Hx^{k+1}\|^2 - 2(y - Hx^{k+1})^T H(x - x^k) \\ &\quad + \|H(y - Hx^{k+1})\|^2) + \frac{m}{2} \log(2\pi\sigma_n^2), \end{aligned} \quad (1.3)$$

where, x^k , is the previous estimate of x^{k+1} . The equation is then minimized with respect to x ,

$$\begin{aligned} \min_x (\|y - Hx^k\|^2 - 2(y - Hx^k)^T H(x^{k+1} - x^k) \\ + \|H(y - Hx^k)\|^2), \end{aligned} \quad (1.4)$$

by taking the derivative of Equation 3.8 with respect to x , setting it equal to zero and solving for x which results in:

$$x^{k+1} = x^k - \frac{1}{\alpha} (H^T (y - Hx^k)), \quad (1.5)$$

where α is a convergence term and by Jensen's inequality we restrict α to be ,

$$\alpha \geq \frac{\|H(y - Hx^k)\|^2}{\|(x^{k+1} - x^k)\|^2}. \quad (1.6)$$

In order to speed up the convergence process a two-step ML was used:

$$\begin{aligned} x^{k+1} = x^k + c_1 \left(\frac{x^k + x^{k+1}}{\|H(x^{k+1} - x^k)\|} \right) \\ + c_2 \left(\frac{H^T(y - Hx^k)}{\|H(H^T(y - Hx^k))\|} \right), \end{aligned} \quad (1.7)$$

let,

$$v_1 = \frac{x^k + x^{k+1}}{\|H(x^{k+1} - x^k)\|}, \quad (1.8)$$

and,

$$v_2 = \frac{H^T(y - Hx^k)}{\|H(H^T(y - Hx^k))\|}. \quad (1.9)$$

Expanding $\|y - Hx\|^2$, yields:

$$\|y - Hx\|^2 = yy^T - 2x^T b + x^T Ax. \quad (1.10)$$

In order to solve for c_1 and c_2 in equation 1.7, it is substituted into the equation above and minimize with respect to c_1 and c_2 .

$$\min_{c=(c_1, c_2)} (-2x^T b + x^T Ax), \quad (1.11)$$

this results in the following for c_1 and c_2 :

$$\begin{aligned} & \begin{bmatrix} c_1 \\ c_2 \end{bmatrix} \\ &= \begin{bmatrix} 1 & (Hv_1)^T(Hv_2) \\ v_1(H^T(y - Hx^k)) & 1 \end{bmatrix}^{-1} \\ & \times \begin{bmatrix} v_1(H^T(y - Hx^k)) & v_2(H^T(y - Hx^k)) \end{bmatrix}. \end{aligned} \quad (1.12)$$

These resulting values for c_1 and c_2 , are then substituted into 1.7 to solve for the reconstructed image, x .

A.2 Regularized Maximum Likelihood

Regularized Maximum Likelihood restricts the values of the reconstructed image, thus allowing it not to deteriorate as the iterations are increased. An l_2 regularization term is added to the cost function:

$$p(y|x)p(x) = \frac{1}{(\sqrt{2\pi\sigma_n^2})^m} e^{-\frac{\|y-Hx\|^2}{2\sigma_n^2}} \frac{1}{(\sqrt{2\pi\sigma_x^2})^n} e^{-\frac{\|x\|^2}{2\sigma_x^2}}. \quad (1.1)$$

where, σ_x^2 is the variance of the reconstructed image, x . Ignoring the terms that do not depend on x , up to some constant the negative log-likelihood of the above equation simplifies to:

$$-\log(p(y|x)p(x)) = \frac{1}{2\sigma_n^2} (\|y - Hx\|^2 + \lambda\|x\|^2), \quad (1.2)$$

where the regularization term, λ , equals the following:

$$\lambda = \frac{\sigma_n^2}{\sigma_x^2}. \quad (1.3)$$

Now minimize Equation 3.19 to solve for x :

$$\min_x \|y - Hx\|^2 + \lambda\|x\|^2. \quad (1.4)$$

By taking the derivative, setting equal to zero and solving for, x , the solution for x simplifies to:

$$x = \frac{c}{c + \lambda} \left(x' + \frac{1}{c} H^T (y - Hx') \right), \quad (1.5)$$

where, c , the convergence constant is restricted to be the following:

$$c = \frac{\|H(H^T(y - Hx') - \lambda x')\|^2}{\|(H^T(y - Hx') - \lambda x')\|^2}. \quad (1.6)$$

Appendix B - MAP-GMP

Using Bayes' theorem we can incorporate this prior information in the estimation process of the reconstructed image. One possible estimate for the reconstructed image x and the estimation of s , is the maximum a posteriori (MAP) estimate:

$$\operatorname{argmin}_{(x,s)} P(x, y, s|a),$$

$$\operatorname{argmin}_{(x,s)} p(y|x)p(x|s)p(s|a), \quad (1.1)$$

where, the joint probability of (X,Y) can be written as:

$$p(y|x) = \prod_{i=1}^N \frac{1}{\sqrt{2\pi\sigma^2}} e^{-\frac{(y_i - (Hx)_i)^2}{2\sigma_{img}^2}}. \quad (1.2)$$

Equation 1.1 can be solved by taking the negative log likelihood ($-\log(P(x, y, s|a))$) then minimizing with respect to x , which simplifies to the following:

$$\operatorname{argmin}_{x_i} \sum_{i=1}^N \frac{(y_i - (Hx)_i)^2}{2\sigma_x^2} + \sum_{s=1}^S \sum_{i=1}^N \frac{(x_i - \mu_s)^2}{2\sigma_s^2} I(s_i = s), \quad (1.3)$$

where, σ_x is the standard deviation of the noise on x . Rewriting equation 1.3 in vector form and simplifying yields:

$$\min_x \left(\frac{(y - Hx)^T (y - Hx)}{2\sigma_x^2} + \frac{1}{2} (x - \mu_s)^T \underbrace{\text{diag} \left(\begin{array}{ccc} \frac{1}{\sigma_{s_i}} & \dots & 0 \\ \vdots & \ddots & \vdots \\ 0 & \dots & \frac{1}{\sigma_N} \end{array} \right)}_D (x - \mu_s) \right). \quad (1.4)$$

The matrices, μ_s is an $N \times N$ image, each pixel of that image contains a value of μ to which that pixel is mapped to by the indicator function $I(s)$. The matrix D , is a diagonal matrix with the σ_s along the diagonal. Expanding Equation 1.4 and lumping like terms results in the following:

$$\min_x \frac{1}{2\sigma_x^2} yy^T + \frac{1}{2} x^T \left(\frac{H^T H}{\sigma_x^2} + D \right) x - 2x^T \left(\frac{H^T y}{\sigma_x^2} + D\mu_s \right) + \mu_s^T D\mu_s. \quad (1.5)$$

In order to minimize equation 1.5 the derivative with respect to x is taken and the solution is set equal to zero:

$$\frac{d}{dx} \left(x^T \left(\frac{H^T H}{\sigma_x^2} + D \right) x - 2x^T \left(\frac{H^T y}{\sigma_x^2} + D\mu_s \right) \right) = 0. \quad (1.6)$$

Let,

$$A = \left(\frac{H^T H}{\sigma_x^2} + D \right), \quad (1.7)$$

$$b = \left(\frac{H^T y}{\sigma_x^2} + D\mu_s \right). \quad (1.8)$$

Substituting the values for A and b , equation 1.6 can be rewritten as:

$$\frac{d}{dx} (x^T Ax - 2x^T b) = 0. \quad (1.9)$$

The derivative of 1.9 is found and we solve for x ,

$$x = 2A^{-1}b. \quad (1.10)$$

Although this is a solution for x we are unable to utilize it because the inverse of A is unknown, since the matrix is too large or it does not exist. In order to work around this solution we re-write $x^T Ax$ to be the following:

$$x^T Ax = (x^k - x^{k+1} + x^{k+1})^T A(x^k - x^{k+1} + x^{k+1}). \quad (1.11)$$

Where x^k is the previous iteration of x^{k+1} , expanding 4.15,

$$\begin{aligned} (x^k)^T Ax &= c\|x^{k+1} - x^k\|^2 + 2(x^{k+1} - x^k)^T Ax^{k+1} \\ &\quad + x^{k+1} Ax^{k+1}, \end{aligned} \quad (1.12)$$

where c , by the Rayleigh Quotient is defined as:

$$c \geq \frac{(x^{k+1} - x^k)^T A(x^{k+1} - x^k)}{\|x^{k+1} - x^k\|^2}. \quad (1.13)$$

Substituting 1.12 into 1.9 and solving for x , yields:

$$x^k = x^{k+1} + \frac{1}{c}(b - Ax^{k+1}). \quad (1.14)$$

Now that we have a solution for x , we must solve for the selection matrix S of the indicator function I , this is done by taking the negative log likelihood of 4.5 ($-\log(P(x, y, s|a))$) and minimizing with respect to s_i :

$$\begin{aligned} \min_{x_i} \sum_{s=1}^S \sum_{i=1}^N \frac{(x_i - \mu_s)^2}{2\sigma_s^2} I(s_i = s) \\ + \sum_{s=1}^S \left(\sum_{N=1}^N I(s_i = s) \right) \log\left(\frac{1}{as}\right) + \sum_{s=1}^S \frac{n_2}{2} \log \sigma_s^2. \end{aligned} \quad (1.15)$$

This results in a discrete equation that simplifies to the following solution of s_i for all $i = \{1, 2, \dots, S\}$:

$$s_i = \arg \min_{s=1,2,\dots,S} \frac{\log(\sigma_s^2)}{2} + \frac{(x_i - \mu_s)^2}{2\sigma_s^2} - \log a_s, \quad (1.16)$$

once all of the S possible solutions for s_i are found, the minimum value of s_i is taken for each individual pixel. The resulting selection matrix, s_i , is then used to find μ_s and

σ_s , two matrices that containing the corresponding mean and standard deviation for each pixel of the image. In order for the algorithm to converge more quickly a two-step MAP was found:

$$x^{k+1} = x^k + z_1 \frac{(b - Ax^k)}{\sqrt{(b - Ax^k)^T A (b - Ax^k)}} + z_2 \frac{(x^{k-1} - x^k)}{\sqrt{(x^{k-1} - x^k)^T A (x^{k-1} - x^k)}} \quad (1.17)$$

Let,

$$v_1 = \frac{(b - Ax^k)}{\sqrt{(b - Ax^k)^T A (b - Ax^k)}}, \quad (1.18)$$

and,

$$v_2 = \frac{(x^{k-1} - x^k)}{\sqrt{(x^{k-1} - x^k)^T A (x^{k-1} - x^k)}} \quad (1.19)$$

This simplifies 4.21 to the following:

$$x^{k+1} = x^k + \underbrace{[v_1 \quad v_2]}_V \underbrace{\begin{bmatrix} z_1 \\ z_2 \end{bmatrix}}_Z. \quad (1.20)$$

Substituting 4.24 into 4.13 and minimizing with respect to (z_1, z_2) :

$$\min_{z=(z_1, z_2)} (x^k + VZ)^T A (x^k + VZ), \quad (1.21)$$

this results in the following for z_1 and z_2 :

$$\begin{bmatrix} z_1 \\ z_2 \end{bmatrix} = [V^T A V]^{-1} \begin{bmatrix} v_1 \\ v_2 \end{bmatrix} (b - Ax^k). \quad (1.22)$$

These resulting values for z_1 and z_2 , are then substituted into 1.1 to solve for the reconstructed image, x .